Title: OGDHL regulates nucleotide metabolism, tumor growth, and neuroendocrine marker expression in prostate cancer

Authors: Matthew J. Bernard[1], Angel Ruiz[1], Johnny A. Diaz[1], Nicholas M. Nunley[2], Rachel N. Dove[2], Kylie Y. Heering[2], Sachi Bopardikar[2], Andrea Gallardo[2], Takao Hashimoto[2], Raag Agrawal[3,4], Chad M. Smith[2], Blake R. Wilde[4,5], Nedas Matulionis[5], Helen M. Richards[6], Marina N. Sharifi[7,8], Joshua M. Lang[7,8], Shuang G. Zhao[7,9,10], Michael C. Haffner[6, 11, 12], Paul C. Boutros[3, 4, 13], Heather R. Christofk[4, 5, 14] , Andrew S. Goldstein[2,4,13,14,*]

Affiliations:

1. Molecular Biology Interdepartmental Program, University of California, Los Angeles, Los Angeles, CA 90095, USA
2. Department of Molecular, Cell, and Developmental Biology, University of California, Los Angeles, Los Angeles, CA 90095, USA
3. Department of Human Genetics, University of California, Los Angeles, Los Angeles, CA 90095, USA
4. Jonsson Comprehensive Cancer Center, University of California, Los Angeles, Los Angeles, CA 90095, USA
5. Department of Biological Chemistry, David Geffen School of Medicine, University of California, Los Angeles, Los Angeles, CA 90095, USA
6. Division of Human Biology, Fred Hutchinson Cancer Center, Seattle, WA 98109, USA
7. Carbone Cancer Center, University of Wisconsin-Madison, Madison, WI 53792, USA
8. Department of Medicine, University of Wisconsin-Madison, Madison, WI 53792, USA
9. Department of Human Oncology, University of Wisconsin, Madison, WI 53792, USA
10. William S. Middleton Veterans Hospital, Madison, WI 53792, USA
11. Division of Clinical Research, Fred Hutchinson Cancer Center, Seattle, WA 98109, USA
12. Department of Laboratory Medicine and Pathology, University of Washington, Seattle, WA 98109, USA
13. Department of Urology, David Geffen School of Medicine, University of California, Los Angeles, Los Angeles, CA 90095, USA
14. Eli and Edythe Broad Stem Cell Research Center, University of California, Los Angeles, Los Angeles, CA 90095, USA

* To whom correspondence should be addressed: AGoldstein@mednet.ucla.edu

Abstract

Cells regularly adapt their metabolism in response to changes in their microenvironment or biosynthetic needs. Prostate cancer cells leverage this metabolic plasticity to evade therapies targeting the androgen receptor (AR) signaling pathway. For example, nucleotide metabolism plays a critical role in treatment-resistant prostate cancer by supporting DNA replication, DNA damage response and cell fate decisions. Identifying novel regulators of nucleotide metabolism in treatment-resistant cancer that are dispensable for the health of normal cells may lead to new therapeutic approaches less toxic than commonly used chemotherapies targeting nucleotide metabolism. We identify the metabolic enzyme Oxoglutarate Dehydrogenase-Like (OGDHL), named for its structural similarity to the tricarboxylic acid (TCA) cycle enzyme Oxoglutarate Dehydrogenase (OGDH), as a regulator of nucleotide metabolism, tumor growth, and treatment-induced plasticity in prostate cancer. While OGDHL is a tumor-suppressor in various cancers, we find that its loss impairs prostate cancer cell proliferation and tumor formation while having minimal impact on TCA cycle activity. Loss of OGDHL profoundly decreases nucleotide metabolite pools, induces the DNA damage response marker γ2AX, and alters androgen receptor inhibition-induced plasticity, including suppressing the neuroendocrine markers DLL3 and HES6. Finally, OGDHL is highly expressed in neuroendocrine prostate cancer (NEPC). These findings support an unexpected role of OGDHL in prostate cancer, where it functions to sustain nucleotide pools for proliferation, DNA repair, and AR inhibition-induced plasticity.

52 **Introduction**

53 Cells constantly undergo rapid metabolic changes to respond to external stimuli or local nutrient availability, and
54 to meet biosynthetic demands[1]. This ability to quickly overhaul metabolic networks allows healthy cells to
55 properly integrate signaling, regulate redox homeostasis, and modulate epigenetic substrates that dictate cell
56 fate decisions[2,3]. Due to differences in bioenergetic and metabolite pool needs, these networks are fine tuned in
57 a cell-type specific manner. During oncogenic transformation and disease progression, cancer cells hijack
58 cellular metabolism to evade therapeutic and biological pressures[4,5]. There is a growing appreciation for the
59 reciprocal relationship between cellular lineage and metabolism[6-8]. Perturbation of these metabolic switches
60 dramatically alters cell identity and differentiation. One major function of metabolic enzymes is to generate
61 energy and fuel anabolic growth. In addition, recent findings have indicated that many of these same enzymes
62 also serve non-canonical functions that more directly regulate transcriptional profiles and cellular signaling[9-12].

63

64 Prostate cancer is one of the most common cancers globally, accounting for nearly 1.5 million new cases
65 annually[13]. In the United States alone, there will be more than 35,750 deaths in 2025[14]. Identifying novel
66 strategies for the treatment of advanced prostate cancer is essential for improving outcomes for patients with
67 prostate cancer. Because Androgen Receptor (AR) signaling can promote survival and proliferation of tumor
68 cells[15], most advanced prostate cancers are treated with hormonal therapies that target the AR signaling axis,
69 including Enzalutamide and Apalutamide that directly bind and inhibit AR. While AR inhibitors have improved
70 patient survival for individuals with CRPC[16,17], disease recurrence is nearly universal. One mechanism through
71 which tumor cells adapt to AR blockade is through changes in lineage identity that result in AR-indifferent
72 tumors[18]. Despite recent promising clinical trial results[19], tumors that become resistant to AR blockade currently
73 lack many effective therapeutic options and are almost uniformly lethal[20]. Understanding how cells adapt to AR
74 inhibition and drive resistant phenotypes is essential for developing new therapies for patients with advanced
75 treatment-resistant prostate cancer.

76

77 We previously demonstrated that castration-resistant prostate cancer (CRPC) cells undergo extensive metabolic
78 remodeling in response to prolonged AR inhibition using the antiandrogen drug Enzalutamide[21]. Notably, cells
79 adapting to sustained AR blockade exhibit altered mitochondrial morphology and increased reliance on

80 mitochondrial oxidative metabolism. In prostate cancer, metabolic rewiring occurs concomitantly with the
81 activation of AR-independent lineage programs to evade pharmacological targeting, including acquisition of
82 neuronal, neuroendocrine, and stem-like features[22-26]. We know little about whether treatment-induced changes
83 in metabolism directly regulate treatment-induced plasticity phenotypes, and which enzymes may be involved in
84 this process. The mitochondria serves as a central hub for both bioenergetic production and metabolite pool
85 regeneration, while also influencing cell signaling[27]. Disruption of metabolite pools can induce apoptosis, alter
86 cell fate, and exacerbate cancer progression through the accumulation of oncometabolites. One metabolic
87 enzyme associated with mitochondrial function is Oxoglutarate Dehydrogenase-Like (OGDHL), an isozyme of
88 Oxoglutarate Dehydrogenase (OGDH), which catalyzes the rate-limiting step in the interconversion of alpha-
89 ketoglutarate (a-KG) into succinyl-CoA within the tricarboxylic acid (TCA) cycle. While OGDH is expressed
90 robustly throughout nearly every cellular lineage in the body, OGDHL expression is primarily localized to the
91 brain and liver[28,29]. OGDHL is expressed in various cancer types and displays tumor suppressor properties in
92 kidney, cervical, and pancreatic cancers[30-35]. Despite its aberrant expression across these multiple cancers, our
93 understanding of the function of OGDHL remains poorly characterized. In a few studies, OGDHL has been
94 suggested to modulate immune signaling, lipid metabolism, and DNA damage[30, 34, 35].
95
96 Replication of DNA for proliferation is a strictly regulated process due to the deleterious nature of most mutations.
97 High fidelity replication of nearly 3 billion base pairs is required each time a cell proliferates. Because of this, the
98 DNA repair pathway is critical to maintain cell health and proper proliferation. Many of the most commonly altered
99 tumor suppressor genes, including *Tp53*, *Brca2*, and *Rb1*, are regulators of the DNA damage response and/or
100 serve as cell cycle checkpoints[36-38]. Mutations in these critical genes can usurp the DNA damage regulatory
101 mechanisms and unleash unchecked cell growth, resulting in a more frequent mutation rate and increased
102 susceptibility to oncogenic transformation[39]. Cells accumulate the metabolite precursors required for DNA
103 synthesis through several mechanisms including salvage of ribonucleotides and deoxyribonucleotides from the
104 surrounding microenvironment and through *de novo* synthesis pathways[40]. Rewiring of these metabolic
105 pathways through alternative means during biological and therapeutic pressures serves as one way tumor cells
106 adapt to sustain tumor growth[41]. Precise regulation of these nucleotide pools is paramount for proper RNA and
107 DNA synthesis and repair pathways. Imbalance of these pools can induce replication stress, leading to cell cycle

arrest and apoptosis. Dysregulation of nucleotide pools has also been linked to altered lineage differentiation, which is associated with sensitivity or resistance to targeted therapies. In summary, the intersection of metabolic rewiring and nucleotide metabolism represents an intriguing target for the treatment of aggressive and therapy-resistant cancer subtypes.

Here, we identify the TCA cycle enzyme OGDHL as a regulator of nucleotide metabolism in prostate cancer. OGDHL is elevated in a group of prostate cancer cell lines, patient-derived xenograft (PDX) models, genetically engineered mouse models, and clinical tissues from patients with aggressive, lethal treatment-resistant prostate cancer. Unlike in prior reports of other cancer-types, we did not find evidence for OGDHL as a tumor suppressor or as a regulator of the TCA cycle. Instead, loss of OGDHL expression impairs cell proliferation and tumor formation, while perturbing nucleotide pools and increasing markers of replication stress. We demonstrate that chronic loss of OGDHL restrains the treatment-associated plasticity in response to prolonged AR pathway inhibition, reducing expression of neuroendocrine markers HES6 and DLL3. Our findings suggest that OGDHL plays an unexpected role in prostate cancer, not through TCA cycle activity, but rather through maintenance of nucleotide metabolite pools for DNA replication and repair.

124 **Results**

125

126 **OGDHL regulates cell proliferation and tumor growth in castration-resistant prostate cancer**

127 Having established an important role for the mitochondria following prolonged AR inhibition, we asked whether
128 there are significant transcriptional changes in TCA cycle enzymes following extended (> 6 weeks) Enzalutamide
129 treatment. OGDHL was the most enriched enzyme, exhibiting a greater than 2-fold increase in mRNA expression
130 in Enzalutamide-maintained cell lines compared to control $16D^{CRPC}$ cells (**Figure 1A**). We next verified that
131 OGDHL protein expression was elevated in response to Enzalutamide treatment in two independent models of
132 CRPC, $LuCAP35^{CR}$ and MDA-PCa 180-30[42] (**Figure S1A, S1B)** and found that this upregulation of OGDHL did
133 not correspond to a compensatory downregulation of OGDH (**Figure 1B**). We generated xenograft tumors from
134 MDA-PCa 180-30 cells in NOD-SCID-IL2Rg^{null} (NSG) mice and treated with enzalutamide via daily oral gavage
135 for 2 weeks. OGDHL protein expression was roughly 30% greater in Enzalutamide-treated tumors relative to
136 vehicle treated control tumors (**Figure S1C, S1D).**

137

138 Although the precise physiological role of OGDHL in the TCA cycle has not been well defined, OGDHL has been
139 investigated as a prognostic biomarker for multiple cancers[43,44] and is reported to have tumor-suppressive activity
140 in cervical, pancreatic, kidney, and liver cells[30-35]. To determine the functional role of OGDHL in prostate cancer,
141 we generated constitutive overexpression systems in several prostate cancer cell line models (**Figure S1E**).
142 Forced expression of OGDHL had no impact on tumor cell viability in LNCaP, $16D^{CRPC}$ or PC3 cells (**Figure 1C**).
143 To further investigate the role of OGDHL in prostate cancer, we maintained three parallel sub-lines of $16D^{CRPC}$
144 cells in Enzalutamide to allow them to independently adapt to prolonged AR inhibition. OGDHL protein levels
145 increased in each of these lines and this expression increased over time as cells adapted to AR blockade (**Figure**
146 **S1F**). Because increased OGDHL expression seemed to be a consistent cellular response to prolonged AR
147 blockade, we next evaluated how loss of OGDHL influences proliferation. Short hairpin RNA (shRNA)-mediated
148 knockdown of OGDHL in Enzalutamide-maintained $16D^{CRPC}$ and $LuCAP35^{CR}$ cells significantly reduced cell
149 viability (**Figure 1D, S1G-I**). We implanted control and knockdown cells in Matrigel to generate 3D tumoroids
150 and found that OGDHL knockdown significantly reduced tumoroid size, an indicator of proliferative capacity
151 (**Figure 1E-F**).

152 To evaluate the effect of OGDHL loss on tumor formation, we implanted control and OGDHL knockdown
153 Enzalutamide-maintained $16D^{CRPC}$ cells with Matrigel into NSG mice and quantified outgrowths after 4 weeks *in*
154 *vivo*. Tissues recovered from implantation of OGDHL knockdown cells were significantly smaller. Recovered
155 tissues had an average mass of 26.26 +/- 36.24 mg (shOGDHL #1) and 11.34 +/- 5.57 mg (shOGDHL #2)
156 compared to 41.86 +/- 23.67 mg in scrambled control tissues (**Figure 1G, S1J).** Most of the tissues derived from
157 knockdown cells lacked visible outgrowths, so we quantified the percentage of recovered tissues weighing more
158 than the Matrigel alone. Only 33.3% (5/15) of tissues resected from OGDHL knockdown xenografts weighed
159 more than the injection medium alone, compared to 100% (15/15) of tissues resected from control cells ($p =$
160 0.0002), suggesting that OGDHL knockdown cells fail to efficiently grow *in vivo*. We validated reduced protein
161 abundance of OGDHL in the recovered tissues from knockdown cells (**Figure S1K**).
162
163 Interestingly, one outgrowth from OGDHL knockdown cells was greater than five times heavier than any other
164 OGDHL knockdown tissue, suggesting that in rare instances, cells can overcome OGDHL loss to form tumors *in*
165 *vivo*. Taken together, our data suggest that OGDHL does not act as a tumor-suppressor in CRPC, as has been
166 shown in other cancer contexts. These findings indicate that OGDHL supports CRPC growth *in vitro* and tumor-
167 forming capacity *in vivo*.

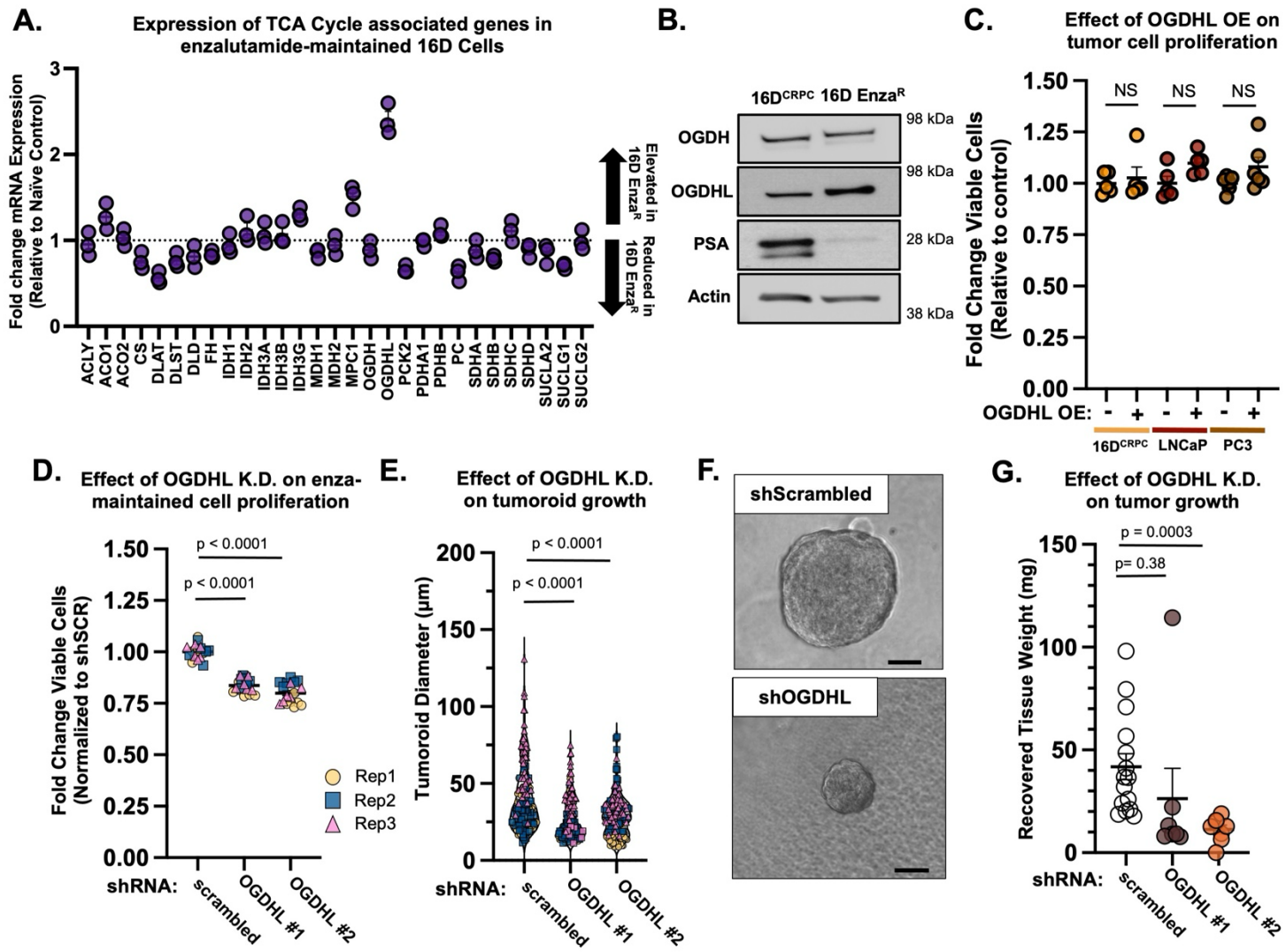

Figure 1: OGDHL Supports proliferation of Enzalutamide-resistant Prostate Cancer Cells *in vitro* and *in vivo.* **(A)** RNA expression of Canonical TCA cycle genes in Enza-Resistant (Enza^{R}) 16D Cells relative to Enza-naïve cells. **(B)** Western Blot of changes in OGDHL, PSA and OGDH in response to acquisition of Enza-resistance in 16D cells**. (C)** Relative change in cell viability over 48 hours with OGDHL overexpression. Plotted as change in viability relative to control cells. Data from 5 (16D, LNCaP) or 6 (PC3) technical replicates. **(D)** Relative change in cell viability over 48 hours with shRNA-mediated knockdown of OGDHL in Enza-Maintained 16D cells**.** Plotted as change in viability relative to control. Data from 3 biological replicate experiments with 5 technical replicates each. **(E)** Measured tumoroid diameter of Enza-maintained 16D Cells after 2 weeks of 3D culture. Data from 3 biological replicate experiments, >50 tumoroids measured per replicate. **(F)** Representative images of control (shScrambled) and OGDHL knockdown (shOGDHL) tumoroids generated from Enza-Maintained 16D Cells. Scale Bar = 50 µm. **(G)** Measured weights of tissues recovered 4 weeks after implantation *in vivo* from Enza-maintained 16D Cells with control (Scrambled) or OGDHL knockdown. Error bars represent +/- SEM. P-value calculated by unpaired t-test with Welch's Correction

168

169

170 **OGDHL loss suppresses cell cycle-related signatures *in vitro* and *in vivo***

171 Because the role of OGDHL in CRPC seems to differ from its reported function in other cancers, we investigated
172 the effect of OGDHL loss on gene expression by conducting RNA-sequencing in Enzalutamide-Maintained
173 $16D^{CRPC}$ cells. We first asked whether OGDHL loss induces compensatory changes in the expression of closely
174 related TCA cycle enzymes. We found minimal changes in expression of canonical TCA cycle genes (**Figure**
175 **2A**) or a broader list of TCA cycle-associated genes (**Figure S2A**) in response to acute OGDHL loss. We next
176 took an unbiased approach to determine broad transcriptional changes induced by acute knockdown of OGDHL.
177 Significantly upregulated genes were associated with cell stress pathways, including *GADD45A*, *CASP4*, and
178 *TP53INP2*. Significantly downregulated genes were associated with cell cycle and proliferation, such as *CDC20*,
179 *CENPN*, *MYC*, and *TOP2A* (**Figure 2B, 2C**). Gene Set Enrichment Analysis (GSEA) revealed strong
180 downregulation of cell cycle signatures, including the Hallmark gene sets for G2M checkpoint, E2F targets, and
181 Myc Targets at both the gene set and individual gene level (**Figures 2E, S2B**). To confirm results obtained using
182 shRNA-mediated knockdown, we used a CRISPR-Cas9 approach to generate independent OGDHL knockout
183 $16D^{CRPC}$ cell lines that are maintained in Enzalutamide. After validating the knockout cells by Western blot (**Figure**
184 **S2C**), we found that chronic loss of OGDHL did not induce compensatory upregulation of TCA cycle genes
185 (**Figures S2D, S2E**). Similar to acute knockdown of OGDHL, genetic knockout of OGDHL led to a pronounced
186 reduction in G2M checkpoint genes, E2F target genes, and Myc target genes (**Figure 2E**). We implanted OGDHL
187 knockout and control cells in castrated NSG mice to maintain suppression of AR signaling *in vivo* and performed
188 RNA sequencing upon tumor formation. After validating loss of OGDHL protein (**Figure S2F**), we found a strong
189 transcriptional downregulation of G2M checkpoint, E2F targets, and Myc Target genes in knockout cells *in vivo*
190 (**Figure 2F**). Taken together, these data indicate that loss of OGDHL in AR inhibition-resistant CRPC cells
191 represses transcription of cell cycle associated genes and activates transcriptional pathways related to cellular
192 stress.

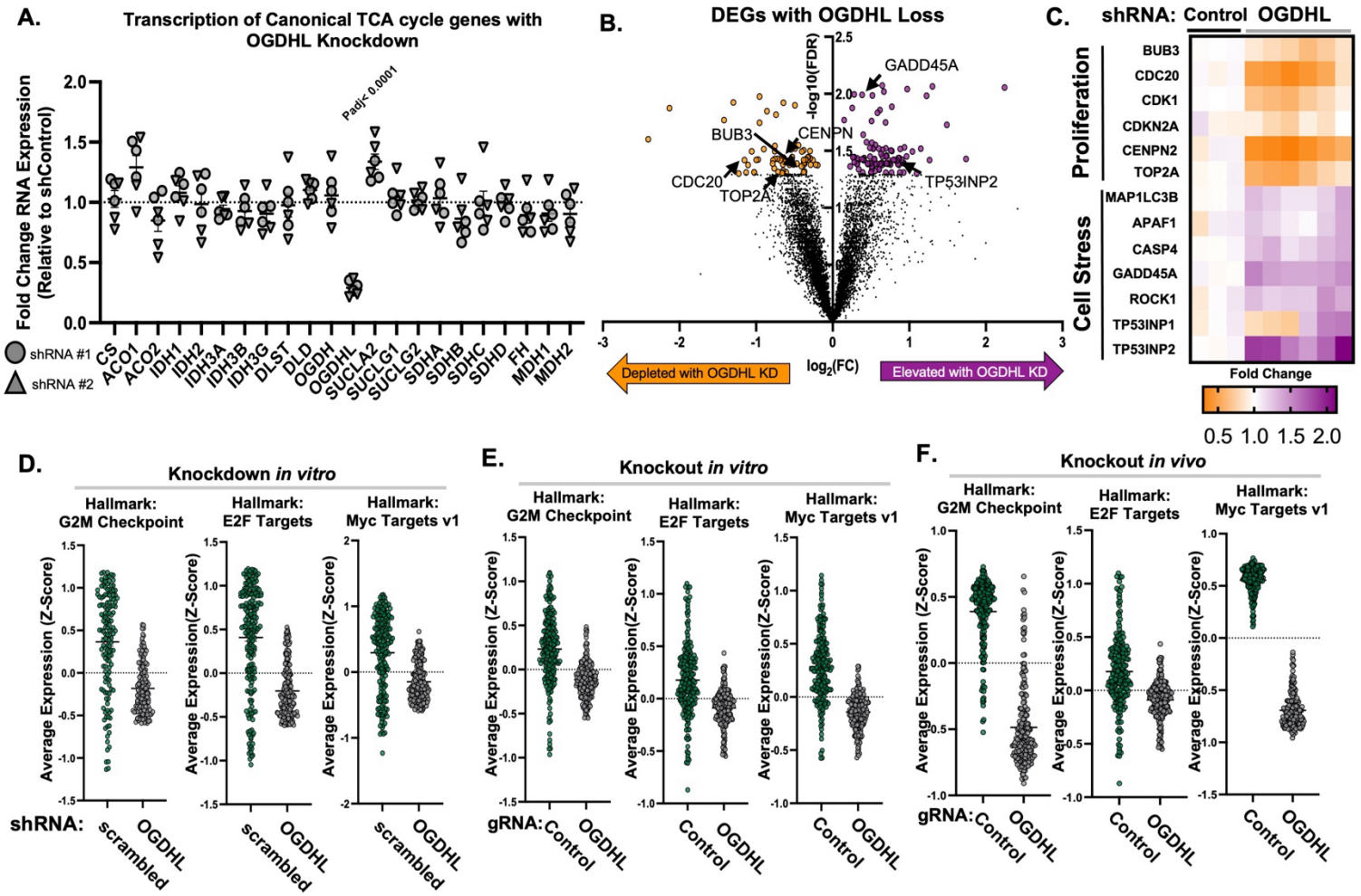

Figure 2: Loss of OGDHL in CRPC cells alters transcription of cell stress and cell cycle associated pathways *in vitro* and *in vivo*. (A) RNA expression of Canonical TCA cycle genes in OGDHL knockdown Enza-maintained 16D Cells *in vitro* normalized to Control knockdown values. Data represented as 3 technical replicates each from 2 shRNAs **(B)** Volcano Plot of Differentially Expressed Genes in shOGDHL Enza-maintained 16D cells relative to control. Color indicates FDR < 0.05 **(C)** Heat Map of isolated proliferation and cell stress genes in control and OGDHL knockdown cells, technical replicates shown. **(D-F)** Average Expression of genes in Hallmark: G2M Checkpoint, E2F Targets, and Myc Targets v1 with Enza-Maintained 16D cells with acute knockdown of OGDHL *in vitro* **(D)**, in OGDHL CRISPR knockout cell lines *in vitro* **(E)**, and in tumors formed from OGDHL knockout cells **(F)**. Data shown is average Z scores from 3 control replicates and 6 Knockdown/Knockout replicates *in vitro* or 5 control and 4 Knockout replicates *in vivo.* Error bars represent +/- SEM. Adjusted P values were calculated by applying the Benjamini-Hochberg procedure for multiple hypothesis testing to p-values corresponding to 2-tailed t-tests.

193

194

195 **OGDHL regulates nucleotide biosynthesis in AR-inhibition resistant prostate cancer**

196 Due to the unexpected effect of OGDHL loss on transcription of proliferation and cellular stress genes, we next
197 set out to determine the metabolic function of OGDHL in prostate cancer cells. OGDHL is predicted to form a
198 complex with dihydrolipoyl succinlyltransferase (DLST) and dihydrolipoyl dehydrogenase (DLD) to catalyze the
199 conversion of alpha-ketoglutarate (a-KG) into succinyl-CoA in the TCA cycle[45]. To measure changes in nutrient
200 utilization, we conducted heavy-isotope nutrient tracing experiments using U-^{13}C Glucose and U-^{13}C Glutamine
201 for 24 hours (**Figure 3A**) in Enzalutamide-Maintained 16D^{CRPC} cells with OGDHL knockdown. OGDHL loss did
202 not lead to an accumulation of heavy-isotope labeled a-KG (**Figure 3B**) or a reduction in labeled carbons
203 downstream of a-KG from either glucose or glutamine (**Figure S3A-S3C**). These findings suggest that OGDHL
204 plays a limited role in regulating the incorporation of glucose or glutamine-derived metabolites into the TCA cycle
205 in CRPC cells, possibly due to the functional redundancy with OGDH.

206

207 We next attempted to identify other metabolic consequences of acute OGDHL loss. Many of the significantly
208 depleted metabolites were involved in pyrimidine biosynthesis and nucleotide homeostasis (**Figure 3C**). Across
209 multiple biological replicates of Enzalutamide-maintained prostate cancer cells, OGDHL loss consistently led to
210 a depletion of nucleotide phosphates (**Figure 3D**) and reduced abundance of certain biosynthetic intermediates
211 of nucleotide synthesis including dihydroorotate and Phosphoribosyl pyrophosphate (PRPP; **Figure S3D, S3E**).
212 Glucose can be incorporated into *de novo* synthesized nucleotides through conversion to a ribose backbone via
213 the pentose phosphate pathway (**Figure 3A**). We found that acute OGDHL loss reduced carbon labeling into
214 nucleotide phosphates from glucose (**Figure 3E**), concurrent with a reduction in nucleotide pools, consistent with
215 decreased activity of the pentose phosphate pathway and diminished *de novo* nucleotide synthesis.

216

217 To understand how chronic loss of OGDHL influences cellular metabolism, we conducted heavy-isotope nutrient
218 tracing experiments in OGDHL knockout cell lines. When we tracked glucose incorporation into the TCA cycle,
219 we found that labeling of a-KG was similar to labeling of other TCA cycle intermediates (**Figure S3F).** Further,
220 OGDHL knockout did not alter labeling from glutamine into the TCA cycle, through either the oxidative (**Figure**
221 **S3G**) or reductive carboxylation (**Figure S3H)** pathways. Much like in response to acute knockdown, metabolic
222 profiling of OGDHL knockout cells revealed a reduction in abundance of ribonucleotides and

deoxyribonucleotides (**Figure 3F**). Taken together, our metabolic data indicate that the main metabolic consequence of OGDHL loss in CRPC cells is not altered TCA cycle metabolism, but rather depletion of nucleotide pools, at least in part through slowed *de novo* nucleotide synthesis.

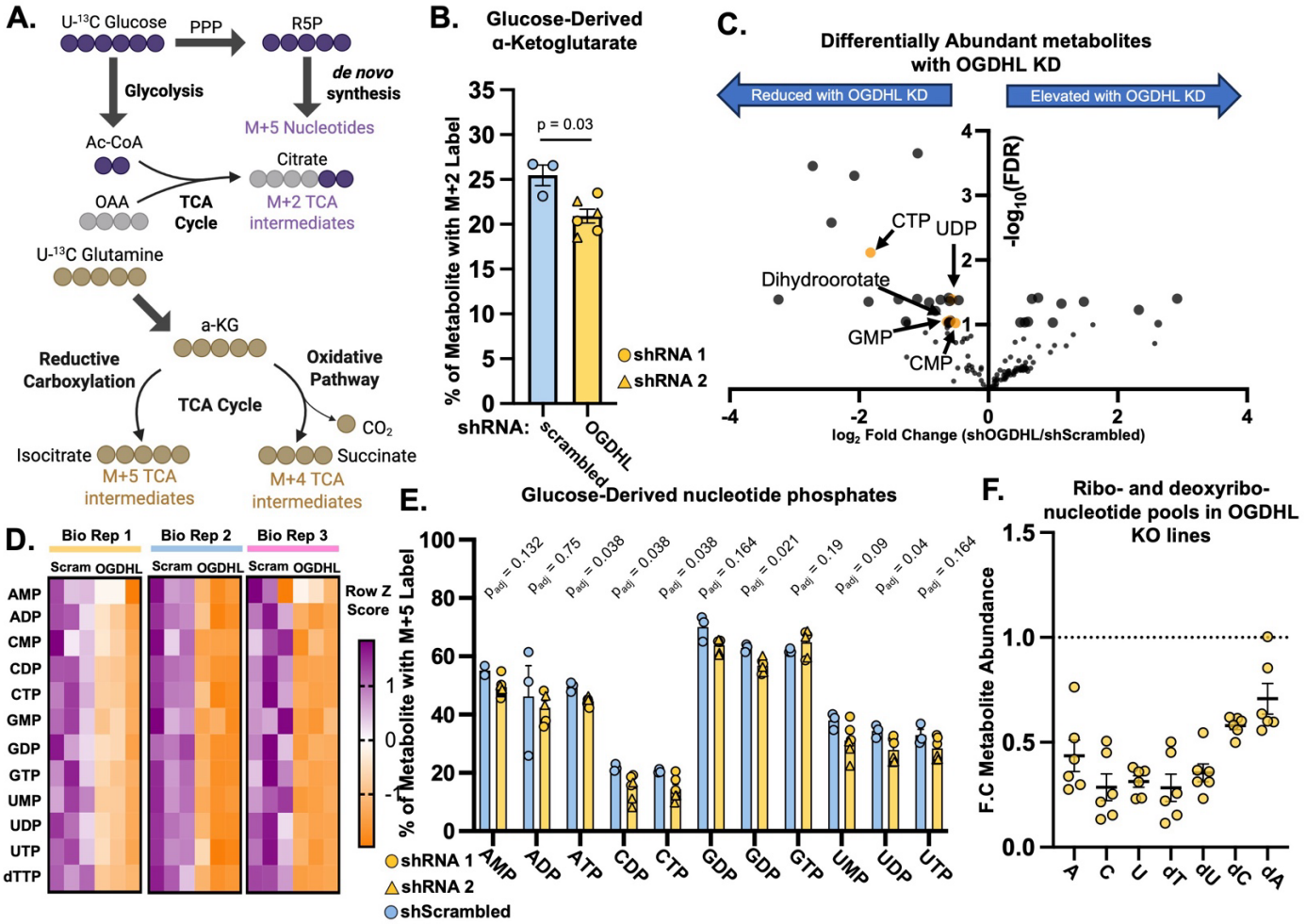

Figure 3: OGDHL loss perturbs nucleotide pools and glucose incorporation into nucleotides. (A) Schematic of heavy-isotope (U-^{13}C Glucose or U-^{13}C Glutamine) nutrient tracing into TCA cycle and nucleotide metabolic intermediates **(B)** M + 2 labeled α-ketoglutarate from U-^{13}C glucose in control or OGDHL knockdown Enza-maintained 16D cells. Data Represents 3 technical replicate experiments for each of 2 shRNAs. **(C)** Volcano Plot of differentially abundant metabolites from metabolic profiling of Enza-maintained 16D Cells with OGDHL or control knockdown. Highlighted metabolites are nucleotide synthesis intermediates. Line indicates FDR = 0.05. **(D)** Heatmap of nucleotide phosphate abundance in OGDHL knockdown and control knockdown Enza-maintained 16D cells. Data represented as row z scores from 3 technical replicates from each of 3 biological replicate lines. **(E)** M + 5 labeling of nucleotide phosphates derived from U-^{13}C glucose in control and OGDHL knockdown Enza-maintained 16D cells. **(F)** Abundance of ribonucleotides and deoxyribonucleotides in OGDHL knockout Enza-maintained 16D Cells relative to control knockout lines. Dashed line represents equivalent abundance. Error bars represent +/- SEM. Adjusted P values were calculated by applying the Benjamini-Hochberg procedure for multiple hypothesis testing to p-values corresponding to 2-tailed t-tests.

228 **OGDHL regulates DNA repair and cell stress pathways in prostate cancer**

229 Nucleotide imbalance has a profound impact on cellular proliferation, cell cycle progression, and DNA damage
230 machinery[46]. As we found that loss of OGDHL diminished nucleotide pools and reduced glucose incorporation
231 into newly synthesized nucleotides, we evaluated expression of nucleotide metabolism genes. Genetic knockout
232 of OGDHL *in vitro* and *in vivo* reduces expression of critical *de novo* nucleotide synthesis and salvage genes
233 including Carboamoyl-Phosphate Synthase 2 (*CAD*), Dihydroorotate Dehydrogenase (*DHODH*), Uridine
234 monophosphate synthetase (*UMPS*), Hypoxanthine phosphoribosyltransferase 1 (*HPRT1)* and Adenine
235 phosphoribosyl transferase (APRT) (**Figure 4A, 4B, S4A, S4B**). More broadly, OGDHL knockout reduced
236 expression of genes in the KEGG Pyrimidine Metabolism gene set (**Figure 4C**). Similarly, we found that acute
237 knockdown of OGDHL in Enzalutamide-maintained $16D^{CRPC}$ cells reduced transcription of *de novo* pyrimidine
238 synthesis and purine salvage genes (**Figure S4C)**. These data indicate that diminished nucleotide abundance
239 following the loss of OGDHL expression in CRPC is likely caused by impaired *de novo* synthesis and nucleotide
240 salvage.

241

242 Depletion of nucleotides can cause genomic instability and trigger replication stress, leading to double stranded
243 DNA breaks, cell cycle arrest and apoptosis[47,48] OGDHL has been implicated as a potential regulator of DNA
244 damage in cancer[35,49]. Thus, we wondered whether loss of OGDHL may cause increased replication stress.
245 Acute knockdown of OGDHL led to increased transcription of genes in the Hallmark Apoptosis gene set and
246 reduced expression of DNA repair pathway genes (**Figure 4D, 4E).** In addition to transcriptional hallmarks of
247 replication stress, we also identified that knockdown of OGDHL *in vitro* led to increased abundance of γH2AX
248 (**Figure 4F**), a sensitive marker of double stranded DNA breaks and a hallmark of DNA damage[50]. We similarly
249 observed an increase in γH2AX when OGDHL knockdown cells were grown *in vivo* (**Figure 4G, 4H, S4E**).
250 OGDHL loss also reduced expression of the DNA repair pathway genes CHK1 and CHK2 (**Figure S4F).** As DNA
251 damage can induce cell death, we questioned whether OGDHL loss induced higher rates of apoptosis. We found
252 that OGDHL loss increased the percentage of Annexin V^+ cells (**Figure S4G)**. We wondered whether OGDHL-
253 loss induced DNA damage accumulation and apoptosis could be related to depletion of nucleotides.
254 Supplementation with Adenine (A) and Uridine (U) led to reduced γH2AX levels in OGDHL knockdown cells
255 while remaining unchanged in control cells **(Figure S4H)** and reduced apoptosis in the most sensitive knockdown

group **(Figure S4G).** These data suggest that loss of OGDHL in CRPC reduces nucleotide availability, through reduction of nucleotide synthesis and salvage genes, and increases replication stress.

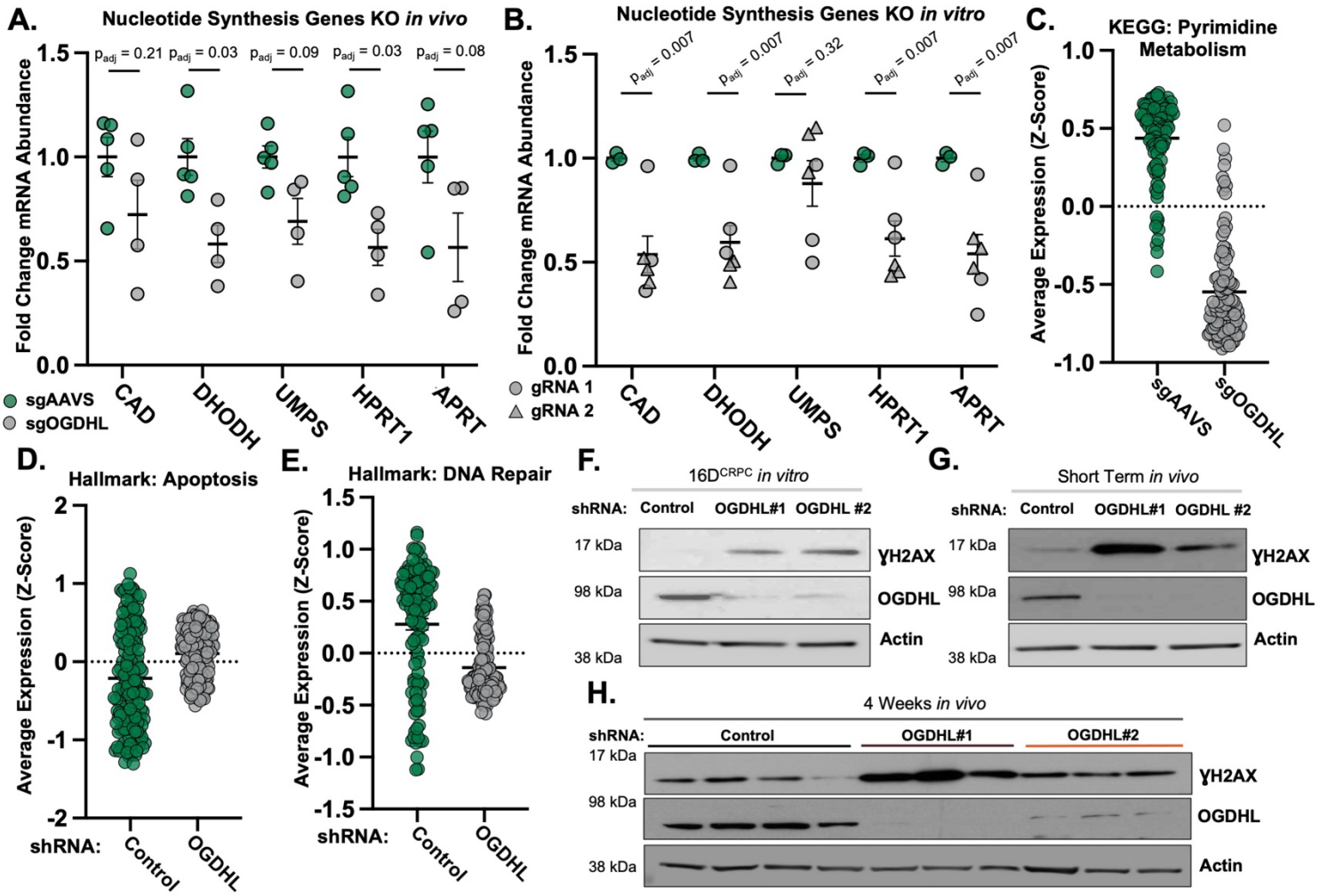

Figure 4: OGDHL Loss reduces nucleotide synthesis gene expression and induces DNA Damage *in vitro* and *in vivo.* (**A-B**) Relative RNA abundance of nucleotide synthesis genes in tumors formed from 16D cells with genetic knockout of OGDHL (n =4) or a control (n = 5) **(A)** or OGDHL knockout cells *in vitro* **(B)**. Data from 3 technical replicates each from 2 gRNAs. **(C)** Average expression of genes in the KEGG: Pyrimidine metabolism gene set in 16D cells with genetic knockout of OGDHL. Data shown represents average Z scores from 3 control replicates and 6 Knockout replicates *in vitro.* **(D-E)** Average expression of genes in the Hallmark: Apoptosis **(D)** and Hallmark: DNA Repair **(E)** gene sets with acute knockdown of OGDHL. Data shown represents average Z scores from 3 control replicates and 6 knockdown replicates *in vitro.* **(F-H**) Western blot of the DNA damage marker γH2AX and OGDHL expression in control and OGDHL knockdown cell lines *in vitro* **(F)**, in cells recovered 4 days after implantation *in vivo* **(G)** and in cells recovered 4 weeks after implantation *in vivo* **(H).** Error bars represent +/- SEM. Adjusted P values were calculated by applying the Benjamini-Hochberg procedure for multiple hypothesis testing to p-values corresponding to 2-tailed t-tests.

260 **OGDHL regulates expression of NEPC drivers *in vitro* and *in vivo***

261 Prolonged AR blockade can induce changes in cell identity as tumor cells adopt AR-indifferent cell fates to adapt
262 to treatment pressure[51]. This process, known as lineage plasticity, can give rise to aggressive and uniformly
263 lethal molecular subtypes, such as neuroendocrine prostate cancer (NEPC)[52]. Because changes in cell fate rely
264 on proper nucleotide balance and DNA damage repair[53,54], we questioned whether loss of OGDHL may alter
265 treatment-induced lineage phenotypes in prostate cancer cells. To understand how OGDHL influences response
266 to prolonged AR blockade, we generated OGDHL knockout lines in $16D^{CRPC}$ cells, then treated them with
267 Enzalutamide for 6 weeks. RNA-sequencing revealed that prolonged Enzalutamide treatment of control cells led
268 to increased expression of genes associated with plasticity phenotypes including Axon Guidance, WNT
269 Signaling, Epithelial-mesenchymal transition, and decreased expression of Androgen Response genes. In
270 contrast, OGDHL knockout impaired the AR blockade-induced upregulation of plasticity-associated gene sets
271 (**Figure 5A-5C, S5A**). Canonical indicators of lineage plasticity and antiandrogen-resistance, including
272 upregulation of *ENO2* (encoding NEPC marker NSE) and *SOX9*[55], were abrogated by loss of OGDHL (**Figure**
273 **S5B, S5C**). OGDHL knockout *in vitro* led to a strong reduction in expression of *HES6* (**Figure 5D)**, an
274 evolutionarily conserved driver of neuronal development[56-58], neuroendocrine differentiation and lineage plasticity
275 in prostate cancer[59-63]. OGDHL knockout also reduced expression of HES6 target genes[64] (**Figure S5D**). We
276 questioned whether this reduction in NEPC markers was a consequence of persistent OGDHL loss or could be
277 induced by acute knockdown of OGDHL. We found that knockdown of OGDHL in Enzalutamide-maintained
278 $16D^{CRPC}$ cells *in vitro* reduced protein expression of HES6 (**Figure S5E)** and transcription of HES6 targets
279 (**Figure S5F),** suggesting that reduced NEPC marker expression is a consistent feature of OGDHL loss.

280

281 We next sought to understand if OGDHL loss could influence lineage plasticity phenotypes *in vivo.* Knockout
282 tumors grown in castrated mice showed statistically significant reductions in transcription of NEPC genes *HES6*
283 and *DLL3* (**Figure 5E, 5F)***.* OGDHL knockout tumors also showed significantly reduced expression of HES6
284 target genes and other gene sets associated with AR blockade-induced plasticity phenotypes (**Figure 5G, S5G,**
285 **S5H**). HES6 protein expression was also reduced following OGDHL knockdown *in vivo* (**Figure 5H, S5I, S5J)**
286 indicating that OGDHL loss modulates expression of NEPC drivers *in vitro* and *in vivo***.** Exogenous
287 supplementation with the nucleotides *in vitro* increased expression of HES6 in OGDHL knockdown cells **(Figure**

288 **S5K)**, suggesting nucleotide depletion may regulate OGDHL-loss induced changes in lineage identity. In
289 summary, these data suggest that OGDHL influences AR-blockade induced lineage plasticity phenotypes
290 including expression of drivers of progression to NEPC.

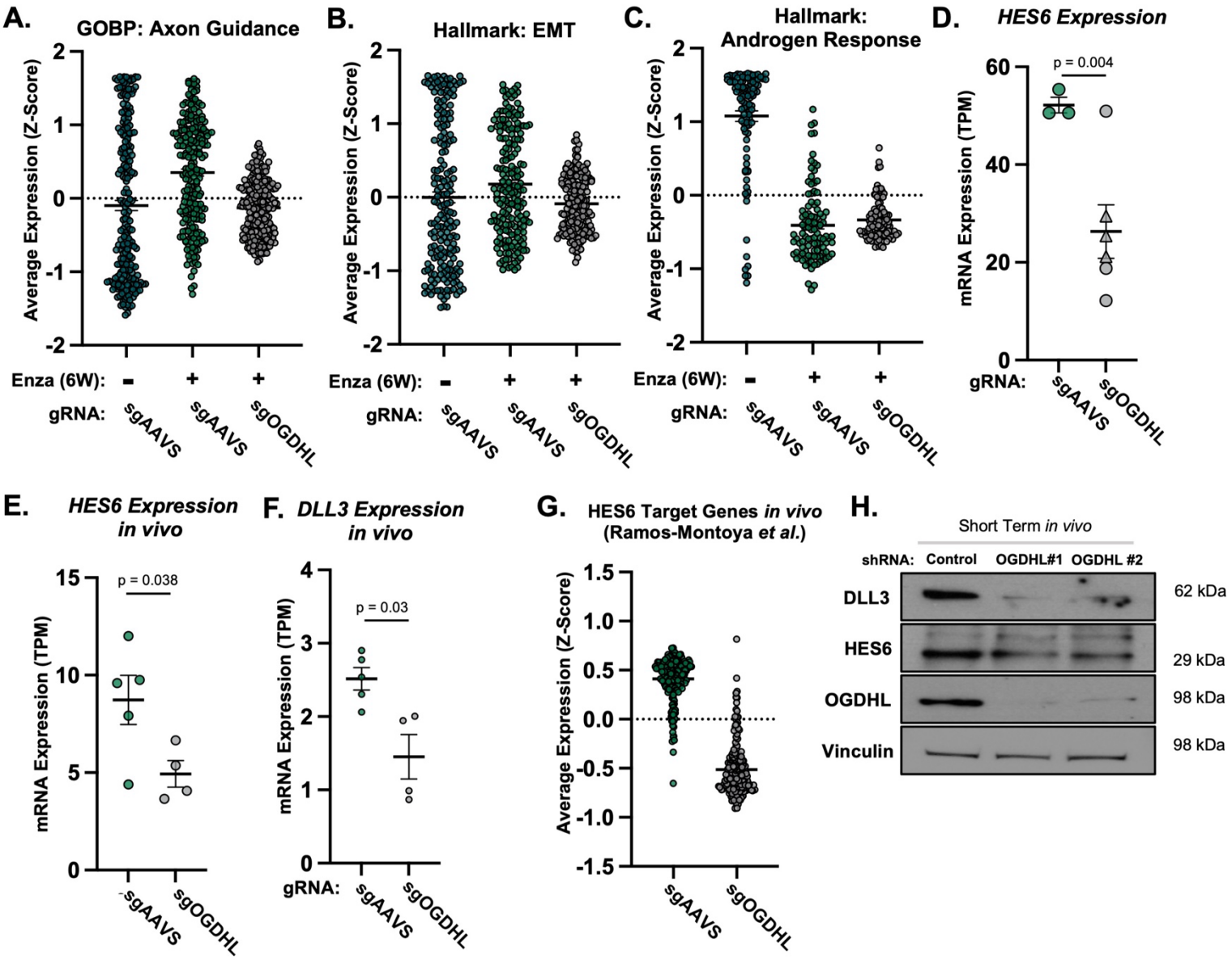

Figure 5: OGDHL mediates lineage plasticity phenotypes and NE marker expression in prostate cancer. (A-C) Average expression of genes in Gene Ontology Biological Pathway Gene Set: Axon Guidance **(A)**, Hallmark: Epithelial Mesenchymal Transition (**B**) and Hallmark: Androgen Response **(C)** gene sets in 16D cells with CRISPR-Cas9 mediated genetic knockout of OGDHL allowed to adapt to enzalutamide for 6 weeks *in vitro.* Data shown represents average Z scores from 3 control replicates (+/- Enza) and 6 Knockout replicates (+Enza) *in vitro.* **(D)** mRNA Expression of NEPC driver gene *HES6* in 16D Cells with genetic knockout of OGDHL cultured *in vitro.* **(E and F)** mRNA expression of NEPC driver gene *HES6* (E) and NEPC-associated gene *DLL3* **(F)** tumors formed from 16D cells with genetic knockout of OGDHL (n =4) or a control (n = 5). **(G)** Average expression of HES6 Target genes (Curated by Ramos-Montoya *et al.* 2014) in tumors formed from 16D cells with genetic knockout of OGDHL (n =4) or a control (n = 5). **(H)** Western Blot of NEPC genes DLL3 and HES6 in in control and OGDHL knockdown cell lines cells recovered 4 days after implantation *in vivo.* Error bars represent +/- SEM. P-value calculated by unpaired t-test with Welch's Correction.

291 **OGDHL expression is associated with Neuroendocrine differentiation in prostate cancer**

292 As we found that OGDHL loss influenced treatment-associated lineage phenotypes, we next set out to identify
293 the expression pattern of OGDHL in advanced prostate cancer. We first interrogated TCA cycle enzyme
294 expression in a series of murine models of prostate cancer progression driven by loss of tumor suppressors
295 *Pten*, *Rb1* and *Tp53*[65]. Notably, the combined loss of *Pten* and *Rb1* (double knockout, DKO) or all three genes
296 together (triple knockout, TKO) promotes a loss of luminal features and a gain of markers associated with NEPC.
297 Among all TCA cycle genes evaluated, OGDHL was the most prominently associated with disease progression
298 and plasticity (**Figure 6A**). OGDHL expression was greater than 10-fold higher in the NEPC-like TKO (Rb1
299 null;Tp53-null;PTen-null) tumors compared to the more luminal-like Pten-knockout tumors (**Figure 6B**). We next
300 questioned whether this correlation with prostate cancer plasticity was also observed in clinical human prostate
301 cancer and in patient-derived xenograft tumors. In RNA sequencing data collected from clinical CRPC patients[66],
302 we found that OGDHL expression was nearly 15-fold higher in patients with NEPC compared to CRPC-
303 adenocarcinoma (**Figure 6C).** In the Stand Up 2 Cancer metastatic CRPC dataset[67,68], OGDHL expression was
304 highest in tumors with NE features, regardless of AR expression/activity, while OGDHL expression was lowest
305 in tumors lacking NE features (**Figure 6D)**. Similar results were observed in the University of Washington rapid
306 autopsy metastatic cohort[69] (**Figure 6E)** and in the LuCAP PDX series[70] (**Figure 6F)** where OGDHL expression
307 was highest in the NE+ AR- subset of tumors. Sharifi *et al.* recently defined mCRPC phenotypes based on RNA
308 sequencing of circulating tumor cells, demonstrating that NE and LumB subtypes are associated with the shortest
309 overall survival[71]. We found that OGDHL mRNA was detectable in CTCs and its expression was highest in the
310 NE+ and LumB subtypes (**Figure 6G**). To ensure OGDHL expression was not suppressed by AR, we evaluated
311 OGDHL expression in patients treated with Androgen Deprivation Therapy (ADT)[72-74]. We found that OGDHL
312 expression was reduced in patients following ADT treatment in both paired and unpaired data sets (**Figure S6A-**
313 **S6C).** Collectively, these data suggest that OGDHL is not specifically associated with AR repression but rather
314 with plasticity and NE differentiation in CRPC.

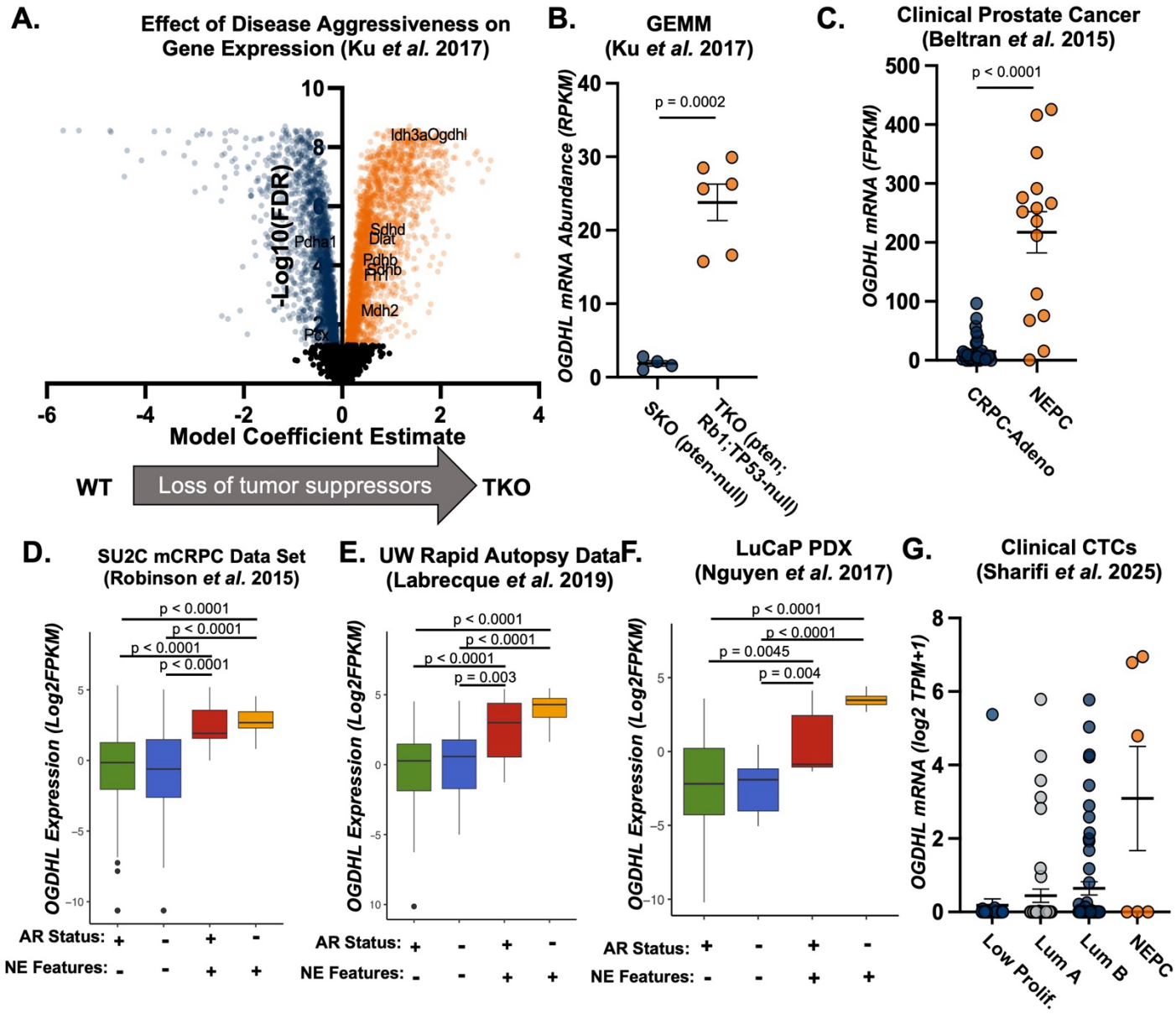

Figure 6: OGDHL expression is elevated in Neuroendocrine Prostate Cancer. (A) Volcano Plot of differentially expressed genes correlated with disease progression in the Ku *et al.* GEMM data set[65]. Highlighted genes correspond to an FDR < 0.05. Gene names of the top 10 differentially regulated TCA cycle genes are displayed. **(B and C)** *OGDHL* mRNA expression in a GEMM model[65] **(B)** of prostate adenocarcinoma (pten-null (SKO)) (n=4) and NEPC (pten;Rb1;TP53-null (TKO)) (n = 6) or in patients **(C)** with Adenocarcinoma (CRPC-Adeno) or NEPC (From Beltran *et al.*)[66] **(D-F)** *OGDHL* mRNA in clinical metastatic CRPC specimens[68] **(D)**, surgically resected tissue from patients who died from metastatic CRPC[69] **(E)**, and in Patient Derived Xenograft models of CRPC[70] based on AR Expression and NE Features[67,68]. **(G)** *OGDHL* mRNA expression in Circulating Tumor Cells (CTCs) from metastatic CRPC based on profiled subtype from the Sharifi *et al.* dataset[71.] Error bars represent +/- SEM. P-value calculated by unpaired t-test with Welch's Correction.

315

316

317 **Discussion**

318 In this study, we demonstrate that the putative TCA cycle enzyme OGDHL is elevated at the mRNA and protein
319 levels in response to prolonged AR blockade in CRPC cells. Despite its reported function as a tumor-suppressor
320 gene in other cancers[30-35], we find that OGDHL promotes anti-androgen resistant prostate cancer cell
321 proliferation *in vitro* and *in vivo*. While some genes play a consistent role either in suppressing or driving
322 tumorigenesis, many cancer-associated genes have context-dependent functions where they provide protective
323 benefits in some cancer subtypes, while promoting disease progression in others. Among these are epigenetic
324 remodelers such as EZH2 and KDM5A[75-77], signaling factors such as TGFβ[78], and metabolic genes such as
325 PDHA1 and AMPK[79-81]. Our findings suggest that OGDHL represents a context-dependent regulator of cancer
326 progression, promoting cell survival and adaptation to therapeutic pressures in prostate cancer.

327

328 Although the TCA cycle generates intermediate metabolites and biosynthetic precursors to enable metabolic and
329 cellular functions and sustain cell growth, there is a growing appreciation for non-canonical roles of TCA cycle
330 enzymes. Many metabolic enzymes, including the OGDH complex, have been reported to display nuclear
331 localization to rapidly replenish metabolite pools for epigenetic reprogramming, despite their predominant
332 expression in other subcellular compartments[10-12, 82-86]. Metabolites, including those generated through TCA
333 cycle enzymes, are critical substrates for epigenetic regulatory proteins, enabling the deposition and removal of
334 methyl, acetyl, and succinyl marks on histone tails[2,8,87]. This enables cells to rapidly adapt to changes in nutrient
335 availability, respond to extracellular signaling, and promote cell fate decisions. Because of this interconnectivity,
336 there is a reciprocal relationship between cellular metabolism and lineage identity. OGDH complex activity
337 modulates levels of two metabolites that are essential for faithful regulation of differentiation programs. a-KG is
338 a critical intermediate for epigenetic regulation, as it is an obligate substrate for a class of demethylase enzymes
339 called a-KG dependent dioxygenases (KGDDs)[88]. Alternatively, the product of OGDH complex activity, succinyl-
340 CoA, can be used to succinylate lysine residues on histone tails, resulting in changes in chromatin accessibility
341 and gene expression[89,90]. Here, we demonstrate that OGDHL modulates mRNA and protein expression of NEPC
342 markers including DLL3 and HES6, suggesting that OGDHL may promote disease progression in CRPC at least
343 in part through gene regulation. In support of that idea, modulation of OGDHL expression does not markedly
344 alter glucose or glutamine incorporation into TCA cycle intermediates. Instead, OGDHL loss potently depletes

345 nucleotide pools and glucose incorporation into nucleotides, while reducing expression of enzymes that fuel
346 nucleotide synthesis and salvage.
347
348 Proper maintenance of nucleotide pools is essential to enable proliferation, gene expression, and DNA damage
349 repair[91,92]. Accumulation of nucleotides is especially important for the proliferation of tumor cells due to their rapid
350 proliferative demands, thus representing a specific vulnerability. Because of this, nucleotide metabolism is a
351 major target for many clinically deployed cancer therapeutics[93]. However, rewiring of nucleotide metabolism in
352 cancer can facilitate pharmacological resistance and immune cell evasion[94-96]. We find that OGDHL loss in anti-
353 androgen resistant prostate cancer cells depletes nucleotide pools and induces accumulation of γH2AX, a
354 prominent marker of replication stress. These findings are consistent with a previous report that utilized
355 bioinformatic approaches to implicate OGDHL as a potential DNA damage-resistance gene in prostate cancer[48].
356 Interestingly, OGDHL overexpression has been reported to modulate nucleotide pools and induce DNA damage
357 in hepatocellular carcinoma, thereby inhibiting disease progression[35]. This highlights the unique function of
358 OGDHL in prostate cancer progression. In addition to accumulation of γH2AX, we find that OGDHL loss reduces
359 transcription of cell cycle associated genes and increases transcription of apoptotic and cellular stress response
360 genes. We postulate that OGDHL is elevated in response to prolonged AR blockade in order to promote
361 nucleotide homeostasis, which enables sustained proliferation and treatment-induced lineage plasticity. As
362 OGDHL is not highly expressed in benign prostate tissue or localized disease, but is consistently elevated in
363 NEPC, OGDHL may represent a novel therapeutic target for this currently uniformly lethal prostate cancer
364 subtype.
365
366 While our findings highlight the importance of OGDHL in cell survival and lineage plasticity in prostate cancer,
367 many questions remain. Although OGDHL modulates nucleotide metabolism, tumor growth, DNA damage
368 response, and plasticity in CRPC, the mechanisms underlying these roles are still unclear. It is possible OGDHL
369 plays a direct role in epigenetic regulation through enzymatic function in the nucleus, regulating a-KG and
370 succinyl-CoA levels to modulate DNA methylation, histone methylation, and histone succinylation. Identifying
371 OGDHL's precise subcellular localization in antiandrogen-resistant prostate cancer will be important in
372 understanding how it regulates lineage plasticity. Further, as the OGDH complex does not directly modulate

intermediates of *de novo* nucleotide synthesis, more direct mechanistic studies to uncover how OGDHL regulates nucleotide metabolism will be essential. OGDHL is a poorly characterized homolog of a much more broadly expressed and investigated metabolic gene, therefore more careful exploration of the nuances differentiating these two, as well as identifying targetable motifs on OGDHL, are important to clarify its potential as a therapeutic target for currently untreatable prostate cancer subtypes.

380 **Materials and Methods**

381 **Materials Availability**

382 This work did not generate new unique reagents.

383 **Animal Work**

384 All animal work was performed using IACUC approved protocols under the supervision of veterinarians from the
385 Division of Laboratory Animal Medicine at UCLA.

386

387 This method refers to figures 1G, S1J, S1K, 4G, 4H, S4E, 5H, S5I, and S5J.

388 750K Enzalutamide-maintained $16D^{CRPC}$ cells with short-hairpin (shRNA) mediated knockdown of OGDHL or a
389 control vector were implanted subcutaneously with 20 µL of growth factor-reduced Matrigel (Corning: CB-
390 40230C) to form tumors. After 4 days, material was collected from 4 control and 4 knockdown injections and
391 used to generate protein lysate (Short Term *in vivo*). The remaining injections were allowed to grow for 4 weeks,
392 after which material was collected, weighed, and used to generate protein lysate.

393

394 This method refers to figures 2F, S2F, 4A, S4A, 5E-5G, S5G, and S5H.

395 Serial dilutions of 1M, 100K, 10K, and 1K $16D^{CRPC}$ cells with CRISPR-Cas9 mediated genetic knockout of
396 OGDHL were implanted subcutaneously with 20 µL of growth factor-reduced Matrigel (Corning: CB-40230C).
397 Once palpable tumors were measured in at least one mouse per condition (1M Cells: 6 Weeks; 100K Cells: 10
398 Weeks; 10K Cells: 12 Weeks, 1K cells: 16 Weeks), mice were sacrificed, tumors were resected, sectioned, and
399 prepared as lysate or flash frozen for bulk RNA-sequencing.

400

401 This method refers to figure S1C and S1D

402 550K MDa 180-30 PDX cells were implanted subcutaneously with 30 uL of growth factor-reduced Matrigel
403 (Corning: CB-40230C). Tumors were allowed to establish for 19 days, then mice were treated with enzalutamide
404 or DMSO control via oral gavage daily for 14 days. 72 hours after the final treatment, mice were sacrificed,
405 tumors were resected, sectioned, and prepared as lysate.

406

407

408 **Cell Lines, lentiviral transduction and cloning**

409 Cell Lines were routinely tested for mycoplasma and authentication by short tandem repeat analysis (Laragen).
410 Tissue culture plates were coated with 0.01% (v/v) Poly-L-Lysine Solution (Sigma-Aldrich: P4832) diluted 1:20
411 in ddH_2O, then washed with sterile DPBS without Calcium and Magnesium (Gibco: 14-190-20). $16D^{CRPC}$ and
412 LNCaP cells were cultured in RPMI 1640 (Gibco: 22400) supplemented with 10% (v/v) FBS (Sigma-Aldrich:
413 F0926), and 100 units/mL penicillin-streptomycin (Gibco: 15-140-122). Media changes were conducted every 48
414 hours and cells were passaged to fresh tissue culture plates once they reached 90% confluency. PC3 cells were
415 cultured in F-12K media (ATCC 30-2004) supplemented with 10% (v/v) FBS (Sigma-Aldrich: F0926), and 100
416 units/mL penicillin-streptomycin (Gibco: 15-140-122). LuCaP 35CR cells were cultured in Advanced DMEM F-
417 12 supplemented with 1% Glutamax (Gibco 35050061), 10% (v/v) FBS (Sigma-Aldrich: F0926), and 100
418 units/mL penicillin-streptomycin (Gibco: 15-140-122). Enzalutamide treatment was performed by adding 10μM
419 Enzalutamide (Selleck Chemicals: S1250) at each media change.

420

421 Lentivirus with short-hairpin RNA (shRNA) against OGDHL (shOGDHL) or a non-targeting control
422 (shScrambled), Cas9 Guide RNA (gRNAs) targeting OGDHL or an AAVS control, and OGDHL overexpression
423 vector were all obtained from Vectorbuilder (Chicago, IL, USA).

424

425 For Lentiviral transductions, cells were seeded at 30% confluence. After 24 Hours, base media containing
426 lentivirus and 8mg/mL Polybrene (ThermoFisher Scientific: NC0663391). Successful transduction was validated
427 by fluorescence microscopy (fluorescent vectors) or puromycin dihydrochloride selection (1.25 μg/mL) (Gibco:
428 A1113803), 72 H after infection.

429

430 **Tumoroid Culture**

431 This method refers to figure 1E and 1F

432 To generate tumoroids, cells were resuspended in a mixture of growth factor-reduced Matrigel (Corning: CB-
433 40230C) and culture media at a ratio of 7:1 to a density of 500 cells per 80 μL. This mixture was then added to
434 poly-hema coated 24-well culture plates (Corning: 09-761-146) as previously described[97]. Matrigel was allowed
435 to solidify at 37°C for 60 minutes, then 350 μL of RPMI 1640 (Gibco: 22400) supplemented with 10% (v/v) FBS

436 (Sigma-Aldrich: F0926), and 100 units/mL penicillin-streptomycin (Gibco: 15-140-122) was added to the center
437 of the solidified ring. Media was changed every other day. After 2 weeks, at least 50 tumoroids per condition
438 were imaged at 20X magnification and diameter was measured.
439
440 MDA-PCa 180-30 PDX tumors were maintained by serial implantation of 20 – 80 mg of minced tumor tissue.
441 Tumors were collected and cryopreserved. Upon thawing, tumor sections were mechanically dissociated and
442 embedded in Matrigel rings to establish *ex vivo* tumoroids. Tumoroids were maintained in Human Organoid
443 Media[98]. To passage tumoroids, media was removed and matrigel containing tumoroids was dissociated by
444 resuspension in Advanced DMEM-F12 (Gibco: 12-634-010) containing 1 mg/mL Dispase II (Gibco: 17-105-041)
445 and 10μM p160 ROCK-inhibitor Y-27632 2HCl (Selleck Chemicals: S1049). This mixture was incubated at 37°C
446 for 1 hour with constant rocking. Following dissociation, cells were pelleted by centrifugation at 800xG for 5
447 minutes, then resuspended in prewarmed 0.05% Trypsin-EDTA, Phenol Red (Gibco: 25-300-120) and pipetted
448 to homogenize. After 1 minute, media was added to quench the trypsinization, and cells were plated into Matrigel
449 rings as above. To treat with enzalutamide, Human organoid media containing 10 μM Enzalutamide was added
450 for 1 week, with fresh media supplied every other day.
451
452 ***In vitro* metabolic profiling and U-^{13}C isotope tracing**
453 This method refers to figures 3C, 3D, and S3E.
454 Enzalutamide-Maintained 16D cells harboring genetic knockdown (shRNA) OGDHL or a control vector were
455 seeded in a 6-well plate (Corning: 07-200-83) at 325K cells/well. After 48 hours, cells were washed with PBS,
456 then provided with glucose-free RPMI 1640 (Gibco: 11-879-020) supplemented with 11 mM U-^{13}C glucose
457 (Cambridge Isotope Labs: CLM-1396), 10% (v/v) FBS (Sigma-Aldrich: F0926), and 100 units/mL penicillin-
458 streptomycin (Gibco: 15-140-122).
459 24 hours after the addition of heavy-isotope labeled media was added, cells were harvested and extracted using
460 previously described methods[21]. In short, cells were placed on ice and washed with ice-cold 150 mM ammonium
461 acetate, pH 7.3, then immediately treated with 500 μL of 80% MeOH (v/v) containing 10nM
462 trifluoromethanesulfonate (internal standard). Cells were then scraped and transferred to a 1.7 mL
463 microcentrifuge tube, vortexed 3 times on ice then centrifuged at 17,000xg for 5 minutes. The supernatant was

464 transferred to ABC glass vials (DWK Life Sciences Wheaton 03-410-151) and dried using the EZ-2Elite
465 Evaporator (Genevac). Samples were stored at -80°C until analysis by LC-MS.
466
467 Dried metabolites were reconstituted in 100 µL of a 50% acetonitrile (ACN) 50% dH20 solution. Samples were
468 vortexed and spun down for 10 min at 17,000g. 70 µL of the supernatant was then transferred to HPLC glass
469 vials. 10 µL of these metabolite solutions were injected per analysis. Samples were run on a Vanquish (Thermo
470 Scientific) UHPLC system with mobile phase A (20mM ammonium carbonate, pH 9.7) and mobile phase B (100%
471 ACN) at a flow rate of 150 µL/min on a SeQuant ZIC-pHILIC Polymeric column (2.1 × 150 mm 5 µm, EMD
472 Millipore) at 35°C. Separation was achieved with a linear gradient from 20% A to 80% A in 20 min followed by a
473 linear gradient from 80% A to 20% A from 20 min to 20.5 min. 20% A was then held from 20.5 min to 28 min.
474 The UHPLC was coupled to a Q-Exactive (Thermo Scientific) mass analyzer running in polarity switching mode
475 with spray-voltage=3.2kV, sheath-gas=40, aux-gas=15, sweep-gas=1, aux-gas-temp=350°C, and capillary-
476 temp=275°C. For both polarities mass scan settings were kept at full-scan-range = (70-1000), ms1-
477 resolution=70,000, max- injection-time=250ms, and AGC-target=1E6. MS2 data was also collected from the top
478 three most abundant singly-charged ions in each scan with normalized-collision-energy=35. Each of the resulting
479 ".RAW" files was then centroided and converted into two ".mzXML" files (one for positive scans and one for
480 negative scans) using msconvert from ProteoWizard[99]. These ".mzXML" files were imported into the MZmine 2
481 software package[100]. Ion chromatograms were generated from MS1 spectra via the built-in Automated Data
482 Analysis Pipeline[101] (ADAP) chromatogram module and peaks were detected via the ADAP wavelets algorithm.
483 Peaks were aligned across all samples via the Random sample consensus aligner module, gap-filled, and
484 assigned identities using an exact mass MS1(+/-15ppm) and retention time RT (+/-0.5min) search of our in-
485 house MS1-RT database. Peak boundaries and identifications were then further refined by manual curation.
486 Peaks were quantified by area under the curve integration and exported as CSV files. If stable isotope tracing
487 was used in the experiment, the peak areas were additionally processed via the R package AccuCor 2[102] to
488 correct for natural isotope abundance. Peak areas for each sample were normalized by the measured area of
489 the internal standard trifluoromethanesulfonate (present in the extraction buffer) and by the number of cells
490 present in the extracted well.
491

492 This method refers to Figure 3B, 3E, 3F, S3A-3C, and S3F-S3H

493 Enzalutamide-Maintained 16D cells harboring genetic knockdown (shRNA) or knockout (gRNA) of OGDHL or a
494 control vector were seeded in a 6-well plate (Corning: 07-200-83) at 325K cells/well. After 48 hours, cells were
495 washed with PBS, then provided with glucose-free RPMI 1640 (Gibco: 11-879-020) supplemented with 11 mM
496 U-^{13}C glucose (Cambridge Isotope Labs: CLM-1396), 10% (v/v) FBS (Sigma-Aldrich: F0926), and 100 units/mL
497 penicillin-streptomycin (Gibco: 15-140-122) (for heavy-labeled glucose tracing) or glutamine-free RPMI 1640
498 (Gibco: 21-870-076) supplemented with 2mM U-^{13}C glutamine (Cambridge Isotope Labs: CLM-1822) (for heavy-
499 labeled glutamine tracing), 10% (v/v) FBS (Sigma-Aldrich: F0926), and 100 units/mL penicillin-streptomycin
500 (Gibco: 15-140-122).

501 24 hours after the addition of heavy-isotope labeled media was added, cells were harvested and extracted using
502 previously described methods[21]. In short, cells were placed on ice and washed with ice-cold 150 mM ammonium
503 acetate, pH 7.3, then immediately treated with 500 µL of 80% MeOH (v/v) containing 1 nmol norvaline (internal
504 standard). Cells were then scraped and transferred to a 1.7 mL microcentrifuge tube, vortexed 3 times on ice
505 then centrifuged at 17,000xg for 5 minutes. The supernatant was transferred to ABC glass vials (DWK Life
506 Sciences Wheaton 03-410-151) and dried using the EZ-2Elite Evaporator (Genevac). Samples were stored at -
507 80°C until analysis by LC-MS.

508 To calculate cell number DNA normalization was performed by resuspending the insoluble fraction in 300 uL of
509 lysis solution (0.1M NaCl, 20mM Tris-HCL, 0.1% SDS, and 5mM EDTA in ddH_2O). Samples were then syringed
510 5x using a 25G needle to homogenize. 50uL of each sample was transferred into a 96-well black-walled clear
511 bottom plate (Corning: 07-200-588) and 100 uL of 5µg/mL Hoechst 33342 (ThermoFisher: H1399) in ddH_2O was
512 added. The plate was then incubated for 30 minutes at 37°C in the dark, after which DNA-based fluorescence
513 was measured using a Tecan Infinite M1000 plate reader with 355nm excitation and 465 emission.

514 Dried metabolites were resuspended in 50% ACN:water and 5 ul was loaded onto a Luna 3um NH2 100A (150
515 × 2.0 mm) column (Phenomenex). The chromatographic separation was performed on a Vanquish Flex (Thermo
516 Scientific) with mobile phases A (5 mM NH4AcO, pH 9.9) and B (ACN) and a flow rate of 200 µl/min. A linear
517 gradient from 15% A to 95% A over 18 min was followed by 7 min isocratic flow at 95% A and reequilibration to
518 15% A. Metabolites were detected with a Thermo Scientific Q Exactive mass spectrometer run with polarity
519 switching in full scan mode with an m/z range of 70-975 and 70.000 resolution. Maven (v 8.1.27.11) was utilized

520 to quantify the targeted metabolites by AreaTop using accurate mass measurements (< 5 ppm) and expected
521 retention time previously verified with standards.
522 Values were normalized to cell number. C13 natural abundance corrections were made using AccuCor[102] (N15
523 corrections are made with AccuCor, dual-labeled corrections are made with AccuCor2). Relative amounts of
524 metabolites were calculated by summing up the intensities of all detected isotopologues of a given metabolite.
525 Data analysis was performed using in-house R scripts.
526
527 **Cell Viability Assay**
528 This method refers to figures 1C, 1D, and 1F
529 Cell lines were detached from tissue culture plates using 0.05% Trypsin-EDTA, Phenol Red (Gibco: 25-300-120)
530 at 37°C for 5 minutes then quenched with culture medium, then pelleted by centrifugation, followed by
531 resuspension in base media. 10 µL of the resuspension was then mixed with Trypan Blue (Corning: 25900CI),
532 and cells were counted via hemocytometer.
533 Cells were seeded into duplicate 96-well black-walled clear bottom plate (Corning: 07-200-588) at a
534 concentration of 10K cells/well in 100 µL of base media. Each experiment was completed with between 4 and 6
535 technical replicates per condition. After 16 hours, 100 µL of CellTiter-Glo® Luminescent Cell Viability Assay
536 Reagent (Promega: G7571) was added, the plate was then incubated for 15 minutes at RT, on an orbital shaker.
537 Luminescence was measured using a Tecan Infinite M1000 plate reader with to obtain baseline values. 48 hours
538 later, 100 µL of CellTiter-Glo® Luminescent Cell Viability Assay Reagent (Promega: G7571) was added to the
539 duplicate plate, then incubated for 15 minutes at RT on an orbital shaker, then luminescence was recorded.
540 Difference in luminescence from baseline to the 48 hour timepoint was used as a proxy for changes in cell
541 viability.
542
543 **Apoptosis Assay**
544 This method refers to Figure S4H.
545 Cells were seeded in 6-well tissue culture dishes (Corning: 07-200-83) at 325K cells/well for 48H. Cell culture
546 media and wash media were collected and pooled with quenched trypsin-containing media containing cells and

547 apoptosis analysis was performed using an APC AnnexinV apoptosis detection kit (BioLegend, 640920)
548 according to the provided protocol. Flow cytometry was performed to quantify the percentage of annexin V^+ cells.
549

550 **Immunoblotting**

551 This method refers to figures 1B, S1A-S1H, S1H, S2C, S2F, 4F-4H, S4E-S4G, 5H, S5E, S5I-S5K.
552 Cells were lysed in RIPA buffer (50 mM Tris-HCl pH 8.0, 150 nM NaCl, 1% NP-40, 0.5%Sodium Deoxycholate,
553 0.1% SDS) containing a phosphatase inhibitor cocktail (Halt: 78428) and a protease inhibitor cocktail (Millipore
554 Sigma: 1169749). Sonication was performed with a sonic dismembrator (ThermoFisher Scientific: FB120). For
555 isolation of protein from tumors, small portions were isolated using dissociation with a razor blade, then added
556 to RIPA lysis buffer in bead mill tubes (ThermoFisher Scientific: 15-340-164). The mixture was shaken 60
557 seconds 2x at max intensity using a Bead Mill 4 homogenizer (ThermoFisher Scientific: 15-340-164).
558 Protein concentration was calculated by the Pierce™ BCA Protein Assay (ThermoFisher Scientific: PI23228)
559 according to manufacturer specifications. Samples were run on NuPAGE 4-12% Bis-Tris Gels (ThermoFisher
560 Scientific: NP0335, NP0322) at 200V for 40-50 minutes, then transferred to Immobilon™-P PVDF Membranes
561 (Millipore Sigma: IPVH 00010) at 30V for 60 minutes. Total protein was visualized using the Sypro Ruby protein
562 blot stain (ThermoFisher Scientific: S11791).
563 Membranes were blocked in 5% Milk (LabScientific: M0841) in DPBS without calcium or magnesium (Gibco: 21-
564 600-044) with 0.1% Tween-20 (Fisher: BP337) for at least 1 hour at RT on an orbital shaker. Membranes were
565 then probed with primary antibodies overnight at 4°C, followed by chromophore-conjugated Alexa Fluor 647 anti-
566 mouse (ThermoFisher Scientific: A21235), Alexa Fluor 647 anti-rabbit (ThermoFisher Scientific: A21244), HRP-
567 conjugated anti-mouse (ThermoFisher Scientific: 31437), or anti-rabbit (ThermoFisher Scientific: G-21234)
568 secondary antibodies. Chromophore-conjugated antibodies were detected by fluorescence using a GE Typhoon
569 FLA 9000 Gel Imaging Scanner or Invitrogen IBright 1500. HRP-conjugated antibodies were detected using
570 chemiluminescent detection on film (Fisher: PI34091). Primary antibodies used were β-Actin (Invitrogen: PIMA-
571 1140), Prostate Specific Antigen (PSA) (Cell Signaling: 5877S), OGDHL (Invitrogen MA5-62626), OGDH
572 (Proteintech: 15212-1-AP), Phospho-Histone H2A.X(Ser 139) (γH2AX) (Cell Signaling: 9718S), Vinculin
573 (Abcam: ab129002), HES6 (NovusBio: NBP3-04548), and DLL3 (Cell Signaling: 71804S).
574

575 ***In vitro* RNA Sequencing**

576 This method refers to Figure 2A-E, S2A, S2B, S2C, S2E, 4B-4E, S4B-S4D, 5A-5D, S5A-S5D.

577 Cells were plated into 6-well tissue culture dishes (Corning: 07-200-83) at 325K cells/well. After 48 hours, cells
578 were lifted cell lines were detached from tissue culture plates using 0.05% Trypsin-EDTA, Phenol Red (Gibco:
579 25-300-120) at 37°C for 5 minutes then quenched with culture medium, then pelleted by centrifugation.
580 Supernatant was removed and cells were washed once with sterile DPBS without Calcium and Magnesium
581 (Gibco: 14-190-20), then the supernatant was removed, and cells were flash frozen using Liquid N_2. Cell pellets
582 were maintained at -80°C until submission for sequencing.

583

584 ***In vivo* RNA Sequencing**

585 Small tumor sections were isolated from harvested tumors and flash frozen using flash frozen using Liquid N_2.
586 Tumor sections were maintained at -80°C until submission for sequencing.

587 Libraries for RNA-Seq were prepared with KAPA mRNA HyperPrep Kit. The workflow consists of mRNA
588 enrichment and fragmentation, first strand cDNA synthesis using random priming followed by second strand
589 synthesis converting cDNA:RNA hybrid to double-stranded cDNA (dscDNA), and incorporates dUTP into the
590 second cDNA strand to maintain strand origin information. cDNA generation is followed by end repair to generate
591 blunt ends, A-tailing, adaptor ligation and PCR amplification. Different adaptors were used for multiplexing
592 samples in a half lane. Sequencing was performed on Illumina NovaSeq X Plus for PE 2x50 run. Data quality
593 check was done on Illumina SAV. Demultiplexing was performed with Illumina Bcl2fastq v2.19.1.403 software.

594 The alignment was performed using STAR[103] with human reference genome GRCh38. The Ensembl Transcripts
595 release GRCh38.107 GTF was used for gene feature annotation. For normalization of transcripts counts, TPM
596 normalized counts were generated.

597

598 **Differential gene expression models**

599 This method refers to Figure 6A

600 Differentially expressed gene (DEG) models were fit in R (v4.2.3)(R Core team) using the limma package
601 (v3.54.2) lmFit function[104]. Models were constructed using the log2-transformation of reads per kilobase of
602 transcript per million reads mapped (RPKM) plus one pseudo count as the outcome and an ordinal encoding of
603 genotype as the predictor for each gene independently as follows:

$$Y_i \approx \beta_{0i} + \beta_{1i}X$$

Here Y_i represents a sample outcome vector for an individual gene and β_{0i} represents the model intercept for an individual gene. X represents the genotype vector, which is defined as a z-scored vector of integers representing the varying genotypes in order of disease severity being experimentally modeled. β_{1i} represents the multiplicative change (in doublings) in expression per standard deviation increase in genotypic sate for an individual gene.

Standard errors were moderated using the limma eBayes function[104]. Estimate P-values were adjusted using the Benjamini-Hochberg false discovery rate (FDR) procedure.

RNA Alignment and Quality Control

This method refers to Figure S6A-S6C.

RNA sequencing data, provided as FASTQ files, were obtained for multiple study cohorts (Long et al., NCT01990196, Sharma et al., Wilkinson et al.)[72-74]. All datasets were processed uniformly through metapipeline-RNA (v1.0.0)[105]. Reads were aligned to the GRCh38.14 human reference genome using the STAR aligner (v2.7.11a)[103]. Gene annotations were based on GENCODE Release 45[106]. Initial quality control (QC) assessments for the raw sequencing reads were conducted using FastQC (v0.11.8), which evaluated metrics such as per-base sequence quality, sequence content, and GC content. Post-alignment QC metrics were generated by STAR, including error rates, read length distributions, splicing characteristics, and overall alignment statistics (e.g., percentage of uniquely mapped reads). MultiQC (v1.25) was employed to aggregate and summarize the QC metrics from both FastQC and STAR across all samples[107]. Samples identified as QC outliers using a significance cutoff of 0.05 based on FastQC statistics were removed using OmicsQC[108]. Subsequently, gene and transcript quantification was performed using RSEM (v1.3.3) based on the STAR alignments[109]

Statistical Analysis of OGDHL Gene Expression in patients pre- and post- ADT Therapy

Gene expression levels for *OGDHL* (Oxoglutarate Dehydrogenase L), quantified as Transcripts Per Million (TPM), were used for differential expression analysis. Expression values were $\log_2$-transformed after adding a pseudocount of 1 ($\log_2$(TPM + 1)) prior to statistical testing and visualization. Data from the individual cohorts were aggregated for combined analyses where appropriate.

To compare *OGDHL* expression between 'Pre' and 'Post' conditions using all available samples irrespective of pairing, a two-sided Wilcoxon rank-sum test was performed on the aggregated dataset (n=231 Pre, n=109 Post samples; Fig. S6A).

For samples where paired data were available (i.e., measurements from the same individual under both 'Pre' and 'Post' conditions, n=84 pairs), a two-sided Wilcoxon signed-rank test was employed to assess significant changes in expression within individuals (Fig. S6B). In cases where multiple samples from one condition were present within an individual, their average TPM was taken and considered as a single sample.

The $\log_2$ Fold Change ($\log_2$FC) was calculated for each study cohort and the combined dataset by comparing the average $\log_2$(TPM + 1) expression in the 'Post' condition relative to the 'Pre' condition.

A summary dot plot was generated to visualize the differential expression results across studies (Fig. S6C). In this plot, the size and color of the dots represent the calculated $\log_2$FC. The statistical significance of the comparison for each study (and the combined 'All' dataset), stratified by unpaired and paired analysis types, is indicated by the background shading intensity. P-values obtained from the respective statistical tests (Wilcoxon rank-sum for unpaired, Wilcoxon signed-rank for paired) were adjusted for multiple comparisons across the studies shown using a Bonferroni correction. Darker shading corresponds to a lower adjusted P-value.

All statistical analyses and data visualizations were performed using R version (v4.3.3), BoutrosLab.plotting.general (v7.1.2), data.table (v1.17.0), and cowplot (v1.1.2)[110-113].

Statistical Analysis

Western Blot Quantification

Relative expression was calculated by opening image files in FIJI then inverting to negative. Mean band intensity was measured and plotted as a ratio of protein of interest/loading control. P-values were calculated using unpaired t-tests with Welch's correction.

Statistical analysis of tumor formation rate

Equivalent volume of injection media was weighed as a baseline for input material. Tissue recovered after 4 weeks *in vivo* was weighed and compared to the injection media baseline. P-values for tumor formation was calculated by a 2-tailed Fisher's Exact Test.

658 **Metabolomics Analysis**

659 Metabolite abundance and isotopologue distributions were calculated by normalizing to cell number. Metabolite
660 abundance was measured as the sum of all isotopologues. Fold changes were calculating by averaging
661 metabolite abundance values of control cells relative. False Discovery Rate (FDR) was calculated by applying
662 the Benjamini-Hochberg procedure for multiple hypothesis testing to p-values corresponding to 2-tailed t-tests.
663 Volcano plot was generated by plotting the $\log_2$ transformed fold change and negative $\log_{10}$ transformed FDR
664 values. Heat maps were generated by plotting Row Z scores of metabolite abundance of knockdown cells or
665 control.

666 **RNA sequencing Analysis**

667 Fold changes in RNA expression were calculated by normalizing measured TPM values to the average of the
668 control group. False Discovery Rate (FDR) was calculated by applying the Benjamini-Hochberg procedure for
669 multiple hypothesis testing to p-values corresponding to 2-tailed t-tests. Heat maps were generated by plotting
670 fold change or $\log_2$ transformed fold change in TPM relative to control. Volcano plot was generated by plotting
671 the $\log_2$ transformed fold change and negative $\log_{10}$ transformed FDR values. Gene Set Enrichment Analysis
672 (GSEA) was performed using the Hallmark gene sets from the Molecular Signatures Database (MSigDB) using
673 GSEA (v 4.3.3)[114,115]. Gene sets were gathered from the MSigDB or specified source. Row Z scores were
674 calculated, then plotted as the average for the control or OGDHL knockdown/knockout condition.

675

676 Previously Published Data Sets

677 RNA-sequencing data sets were generated as previously described[21, 65-71]. Bulk RNA-sequencing data that was
678 re-analyzed for this manuscript were obtained as normalized transcript values. Figure 1A was generated from
679 data published by Crowell *et al.*[21] Figures 6A and 6B were generated from data published by Ku *et al.*[65]. Figure
680 6C was generated by NEPC patient tumor data published by Beltran *et al.*[66]. Data for Figures 6D-6E were
681 collected from the StandUp2Cancer mCRPC dataset[67], UW Rapid Autopsy Data Set[69], and the LUCaP PDX
682 Data Set[70], stratification of groups completed by Labraque *et al.*[68]. Data for Circulating Tumor Cells obtained
683 from Sharifi *et al.*[71]. Statistical analysis was completed by unpaired T-Test with Welch's correction.

684

685

686 **Data Accessibility**

687 RNA-Sequencing files were uploaded to Gene Expression Omnibus:

688 Accension IDs: GSE298123, GSE297510, and GSE298381

689

690 Raw metabolomics data is is available at the NIH Common Fund's National Metabolomics Data Repository

691 (NMDR) website, the Metabolomics Workbench[116], *https://www.metabolomicsworkbench.org* where it has been

692 assigned Project IDs 5929 and 5931.

693

694

695

696

697

698

699

700

701

702

703

Acknowledgements

M.J.B. acknowledges the support of the Ruth L. Kirschstein National Research Service Award GM007185 and the NIDDK TL1 DK132768 Award. J.A.D. is supported by the Eugene V. Cota-Robles Fellowship. R.A. is supported by the UCLA-Caltech Medical Scientist Training Program T32GM152342 and the Jonsson Comprehensive Cancer Center Fellowship. M.N.S is supported by the 2022 Point Biopharma Young Valor Investigator award and the Department of Defense PC220240. M.C.H. is supported by the NIH/NCI (R37CA286450), Grant 2021184 from the Doris Duke Charitable Foundation, the V Foundation, the Prostate Cancer Foundation Felix Feng PC-SYNERGY award and the UW/FHCC Institute for Prostate Cancer Research. P.C.B. is supported by the NIH grants P30CA016042, U2CCA271894, R01CA270108 and Department of Defense grants W81XWH2210247 and W81XWH2210751. A.S.G. is supported by UCLA Prostate Cancer Specialized Programs of Research Excellence (SPORE) NCI P50 CA092131, Department of Defense PCRP award HT94252310379, the Mike Slive Foundation for Prostate Cancer Research, the UC Cancer Research Coordinating Committee (C23CR5598), the 2024 Larry & Sherry Benaroya- Prostate Cancer Foundation Challenge Award, the Basser Center for BRCA, the UCLA Eli and Edythe Broad Center of Regenerative Medicine and Stem Cell Research Rose Hills Foundation Innovator Grant, the UCLA Jonsson Comprehensive Cancer Center and Eli and Edythe Broad Center of Regenerative Medicine and Stem Cell Research Ablon Scholars Program, the National Center for Advancing Translational Sciences UCLA CTSI Grant UL1TR001881, STOP CANCER, and the UCLA Institute of Urologic Oncology. The authors would like to thank Dr. Peter Nelson for LuCAP35CR cells and Dr. Nora Navone for MDA-PCa 180-30 patient derived xenograft tissue. We thank the UCLA metabolomics core and members of the Christofk lab for assistance with mass spectrometry and guidance in experimental design. We would also like to thank the UCLA Technology Center for Genomics & Bioinformatics (TCBG) for help with RNA sequencing and data analysis. This work is supported by Metabolomics Workbench/National Metabolomics Data Repository (NMDR) (grant# U2C-DK119886), Common Fund Data Ecosystem (CFDE) (grant# 3OT2OD030544) and Metabolomics Consortium Coordinating Center (M3C) (grant# 1U2C-DK119889). Some figures were created using BioRender: Created in BioRender. Bernard, M. (2025) https://BioRender.com/82da7ku. The funders had no role in study design, data collection and analysis, decision to publish or preparation of the manuscript. We also thank Bill Lowry, Leigh Ellis, Hilary Coller, and Brigitte Gomperts for providing critical feedback and intellectual support during the project.

732

733 **Author Contributions**

734

735 M.J.B., A.R., J.A.D., R.N.D., K.Y.H., S.B., A.G., and T.H. conducted the experiments. M.J.B., N.M.N, C.M.S.,

736 and R.A. completed data quantification and statistical analyses. M.J.B. and A.S.G. designed the experiments,

737 wrote, and edited the manuscript. B.R.W. performed molecular cloning and advised on genetic knockout

738 experiments. N.M. and H.R.C. provided metabolomics expertise, performed mass spectrometry on *in vitro*

739 nutrient tracing experiments, and wrote the related methods section. N.M.N, R.A., H.M.R., M.C.H. and P.C.B.

740 analyzed clinical data sets and provided bioinformatics expertise. M.N.S., J.M.L., S.G.Z., analyzed and

741 provided data corresponding to circulating tumor cells. A.S.G. procured funding and supervised the project.

References

1. Finley LWS. What is cancer metabolism?. *Cell*. 2023;186(8):1670-1688. doi:10.1016/j.cell.2023.01.038

2. Kinnaird A, Zhao S, Wellen KE, Michelakis ED. Metabolic control of epigenetics in cancer. *Nat Rev Cancer*. 2016;16(11):694-707. doi:10.1038/nrc.2016.82

3. Shapira SN, Christofk HR. Metabolic Regulation of Tissue Stem Cells. *Trends Cell Biol*. 2020;30(7):566-576. doi:10.1016/j.tcb.2020.04.004

4. DeBerardinis RJ, Chandel NS. Fundamentals of cancer metabolism. *Sci Adv*. 2016;2(5):e1600200. Published 2016 May 27. doi:10.1126/sciadv.1600200

5. Faubert B, Solmonson A, DeBerardinis RJ. Metabolic reprogramming and cancer progression. *Science*. 2020;368(6487):eaaw5473. doi:10.1126/science.aaw5473

6. Wellen KE, Thompson CB. A two-way street: reciprocal regulation of metabolism and signalling. *Nat Rev Mol Cell Biol*. 2012;13(4):270-276. Published 2012 Mar 7. doi:10.1038/nrm3305

7. Ghosh-Choudhary S, Liu J, Finkel T. Metabolic Regulation of Cell Fate and Function. *Trends Cell Biol*. 2020;30(3):201-212. doi:10.1016/j.tcb.2019.12.005

8. Morrison AJ. Cancer cell metabolism connects epigenetic modifications to transcriptional regulation. *FEBS J*. 2022;289(5):1302-1314. doi:10.1111/febs.16032

9. Yang W, Zheng Y, Xia Y, et al. ERK1/2-dependent phosphorylation and nuclear translocation of PKM2 promotes the Warburg effect [published correction appears in Nat Cell Biol. 2013 Jan;15(1):124]. *Nat Cell Biol*. 2012;14(12):1295-1304. doi:10.1038/ncb2629

10. Sutendra G, Kinnaird A, Dromparis P, et al. A nuclear pyruvate dehydrogenase complex is important for the generation of acetyl-CoA and histone acetylation. *Cell*. 2014;158(1):84-97. doi:10.1016/j.cell.2014.04.046

11. Sharpley MS, Chi F, Hoeve JT, Banerjee U. Metabolic plasticity drives development during mammalian embryogenesis. *Dev Cell*. 2021;56(16):2329-2347.e6. doi:10.1016/j.devcel.2021.07.020

12. Liu X, Si W, He L, et al. The existence of a nonclassical TCA cycle in the nucleus that wires the metabolic-epigenetic circuitry. *Signal Transduct Target Ther*. 2021;6(1):375. Published 2021 Nov 3. doi:10.1038/s41392-021-00774-2

13. Wang L, Lu B, He M, Wang Y, Wang Z, Du L. Prostate Cancer Incidence and Mortality: Global Status and Temporal Trends in 89 Countries From 2000 to 2019. *Front Public Health*. 2022;10:811044. Published 2022 Feb 16. doi:10.3389/fpubh.2022.811044

14. Siegel RL, Kratzer TB, Giaquinto AN, Sung H, Jemal A. Cancer statistics, 2025. *CA Cancer J Clin*. 2025;75(1):10-45. doi:10.3322/caac.21871

15. Rebello RJ, Oing C, Knudsen KE, et al. Prostate cancer. *Nat Rev Dis Primers*. 2021;7(1):9. Published 2021 Feb 4. doi:10.1038/s41572-020-00243-0

16. de Bono JS, Logothetis CJ, Molina A, et al. Abiraterone and increased survival in metastatic prostate cancer. *N Engl J Med*. 2011;364(21):1995-2005. doi:10.1056/NEJMoa1014618

17. Scher HI, Fizazi K, Saad F, et al. Increased survival with enzalutamide in prostate cancer after chemotherapy. *N Engl J Med*. 2012;367(13):1187-1197. doi:10.1056/NEJMoa1207506

18. Beltran H, Hruszkewycz A, Scher HI, et al. The Role of Lineage Plasticity in Prostate Cancer Therapy Resistance. *Clin Cancer Res*. 2019;25(23):6916-6924. doi:10.1158/1078-0432.CCR-19-1423

19. Abida W, Beltran H, Raychaudhuri R. State of the Art: Personalizing Treatment for Patients With Metastatic Castration-Resistant Prostate Cancer. *Am Soc Clin Oncol Educ Book*. 2025;45(3):e473636. doi:10.1200/EDBK-25-473636

20. Sayegh N, Swami U, Agarwal N. Recent Advances in the Management of Metastatic Prostate Cancer. *JCO Oncol Pract*. 2022;18(1):45-55. doi:10.1200/OP.21.00206

21. Crowell PD, Giafaglione JM, Jones AE, et al. MYC is a regulator of androgen receptor inhibition-induced metabolic requirements in prostate cancer. *Cell Rep*. 2023;42(10):113221. doi:10.1016/j.celrep.2023.113221

22. Reina-Campos M, Linares JF, Duran A, et al. Increased Serine and One-Carbon Pathway Metabolism by PKCλ/ι Deficiency Promotes Neuroendocrine Prostate Cancer. *Cancer Cell*. 2019;35(3):385-400.e9. doi:10.1016/j.ccell.2019.01.018

23. Labbé DP, Zadra G, Yang M, et al. High-fat diet fuels prostate cancer progression by rewiring the metabolome and amplifying the MYC program. *Nat Commun*. 2019;10(1):4358. Published 2019 Sep 25. doi:10.1038/s41467-019-12298-z

24. Basu HS, Wilganowski N, Robertson S, et al. Prostate cancer cells survive anti-androgen and mitochondrial metabolic inhibitors by modulating glycolysis and mitochondrial metabolic activities. *Prostate*. 2021;81(12):799-811. doi:10.1002/pros.24146

25. Singh R, Mills IG. The Interplay Between Prostate Cancer Genomics, Metabolism, and the Epigenome: Perspectives and Future Prospects. *Front Oncol*. 2021;11:704353. Published 2021 Sep 29. doi:10.3389/fonc.2021.704353

26. Ahmad F, Cherukuri MK, Choyke PL. Metabolic reprogramming in prostate cancer. *Br J Cancer*. 2021;125(9):1185-1196. doi:10.1038/s41416-021-01435-5

27. Intlekofer AM, Finley LWS. Metabolic signatures of cancer cells and stem cells. *Nat Metab*. 2019;1(2):177-188. doi:10.1038/s42255-019-0032-0

28. Bunik V, Kaehne T, Degtyarev D, Shcherbakova T, Reiser G. Novel isoenzyme of 2-oxoglutarate dehydrogenase is identified in brain, but not in heart. *FEBS J*. 2008;275(20):4990-5006. doi:10.1111/j.1742-4658.2008.06632.x

29. Zhong Y, Gao Y, Zhou D, et al. Structural basis for the activity and regulation of human α-ketoglutarate dehydrogenase revealed by Cryo-EM. *Biochem Biophys Res Commun*. 2022;602:120-126. doi:10.1016/j.bbrc.2022.02.093

30. Sen T, Sen N, Noordhuis MG, et al. OGDHL is a modifier of AKT-dependent signaling and NF-κB function. *PLoS One*. 2012;7(11):e48770. doi:10.1371/journal.pone.0048770

31. Liu Y, Meng F, Wang J, et al. A Novel Oxoglutarate Dehydrogenase-Like Mediated miR-214/TWIST1 Negative Feedback Loop Inhibits Pancreatic Cancer Growth and Metastasis. *Clin Cancer Res*. 2019;25(17):5407-5421. doi:10.1158/1078-0432.CCR-18-4113

32. Dai W, Xu L, Yu X, et al. OGDHL silencing promotes hepatocellular carcinoma by reprogramming glutamine metabolism. *J Hepatol*. 2020;72(5):909-923. doi:10.1016/j.jhep.2019.12.015

33. Dai W, Li Y, Sun W, et al. Silencing of OGDHL promotes liver cancer metastasis by enhancing hypoxia inducible factor 1 α protein stability. *Cancer Sci*. 2023;114(4):1309-1323. doi:10.1111/cas.15540

34. Shi J, Miao D, Lv Q, et al. The m6A modification-mediated OGDHL exerts a tumor suppressor role in ccRCC by downregulating FASN to inhibit lipid synthesis and ERK signaling. *Cell Death Dis*. 2023;14(8):560. Published 2023 Aug 25. doi:10.1038/s41419-023-06090-7

35. Jiang X, Peng J, Xie Y, et al. Oxoglutarate dehydrogenase-like inhibits the progression of hepatocellular carcinoma by inducing DNA damage through non-canonical function. *Cell Death Differ*. 2023;30(8):1931-1942. doi:10.1038/s41418-023-01186-1

36. Roy R, Chun J, Powell SN. BRCA1 and BRCA2: different roles in a common pathway of genome protection. *Nat Rev Cancer*. 2011;12(1):68-78. Published 2011 Dec 23. doi:10.1038/nrc3181

37. Mantovani F, Collavin L, Del Sal G. Mutant p53 as a guardian of the cancer cell. *Cell Death Differ*. 2019;26(2):199-212. doi:10.1038/s41418-018-0246-9

38. Engeland K. Cell cycle regulation: p53-p21-RB signaling. *Cell Death Differ*. 2022;29(5):946-960. doi:10.1038/s41418-022-00988-z Hanahan, D., & Weinberg, R. A. (2011). Hallmarks of cancer: the next generation. *Cell*, *144*(5), 646–674. https://doi.org/10.1016/j.cell.2011.02.013

39. Hanahan D, Weinberg RA. Hallmarks of cancer: the next generation. *Cell*. 2011;144(5):646-674. doi:10.1016/j.cell.2011.02.013

40. Lane AN, Fan TW. Regulation of mammalian nucleotide metabolism and biosynthesis. *Nucleic Acids Res*. 2015;43(4):2466-2485. doi:10.1093/nar/gkv047

41. Villa E, Ali ES, Sahu U, Ben-Sahra I. Cancer Cells Tune the Signaling Pathways to Empower de Novo Synthesis of Nucleotides. *Cancers (Basel)*. 2019;11(5):688. Published 2019 May 17. doi:10.3390/cancers11050688

42. Palanisamy N, Yang J, Shepherd PDA, et al. The MD Anderson Prostate Cancer Patient-derived Xenograft Series (MDA PCa PDX) Captures the Molecular Landscape of Prostate Cancer and Facilitates Marker-driven Therapy Development. *Clin Cancer Res*. 2020;26(18):4933-4946. doi:10.1158/1078-0432.CCR-20-0479

43. Jiao Y, Li Y, Fu Z, et al. *OGDHL* Expression as a Prognostic Biomarker for Liver Cancer Patients. *Dis Markers*. 2019;2019:9037131. Published 2019 Oct 17. doi:10.1155/2019/9037131

44. Mao M, Huang RZ, Zheng J, et al. OGDHL closely associates with tumor microenvironment and can serve as a prognostic biomarker for papillary thyroid cancer. *Cancer Med*. 2021;10(2):728-736. doi:10.1002/cam4.3640

45. Bunik VI, Romash OG, Gomazkova VS. Effect of alpha-ketoglutarate and its structural analogues on hysteretic properties of alpha-ketoglutarate dehydrogenase. *FEBS Lett*. 1991;278(2):147-150. doi:10.1016/0014-5793(91)80104-b

46. Diehl FF, Miettinen TP, Elbashir R, et al. Nucleotide imbalance decouples cell growth from cell proliferation. *Nat Cell Biol*. 2022;24(8):1252-1264. doi:10.1038/s41556-022-00965-1

47. Bester AC, Roniger M, Oren YS, et al. Nucleotide deficiency promotes genomic instability in early stages of cancer development. *Cell*. 2011;145(3):435-446. doi:10.1016/j.cell.2011.03.044

48. Zeman MK, Cimprich KA. Causes and consequences of replication stress. *Nat Cell Biol*. 2014;16(1):2-9. doi:10.1038/ncb2897

49. Challis D, Lippis T, Wilson R, et al. Multiomics analysis of adaptation to repeated DNA damage in prostate cancer cells. *Epigenetics*. 2023;18(1):2214047. doi:10.1080/15592294.2023.2214047

50. Mah LJ, El-Osta A, Karagiannis TC. gammaH2AX: a sensitive molecular marker of DNA damage and repair. *Leukemia*. 2010;24(4):679-686. doi:10.1038/leu.2010.6

51. Hirano D, Okada Y, Minei S, Takimoto Y, Nemoto N. Neuroendocrine differentiation in hormone refractory prostate cancer following androgen deprivation therapy. *Eur Urol*. 2004;45(5):586-592. doi:10.1016/j.eururo.2003.11.032

52. Beltran H, Hruszkewycz A, Scher HI, et al. The Role of Lineage Plasticity in Prostate Cancer Therapy Resistance. *Clin Cancer Res*. 2019;25(23):6916-6924. doi:10.1158/1078-0432.CCR-19-1423

53. Sherman MH, Bassing CH, Teitell MA. Regulation of cell differentiation by the DNA damage response. *Trends Cell Biol*. 2011;21(5):312-319. doi:10.1016/j.tcb.2011.01.004

54. Do BT, Hsu PP, Vermeulen SY, et al. Nucleotide depletion promotes cell fate transitions by inducing DNA replication stress. *Dev Cell*. 2024;59(16):2203-2221.e15. doi:10.1016/j.devcel.2024.05.010

55. Nouri M, Massah S, Caradec J, et al. Transient Sox9 Expression Facilitates Resistance to Androgen-Targeted Therapy in Prostate Cancer. *Clin Cancer Res*. 2020;26(7):1678-1689. doi:10.1158/1078-0432.CCR-19-0098

56. Bae S, Bessho Y, Hojo M, Kageyama R. The bHLH gene Hes6, an inhibitor of Hes1, promotes neuronal differentiation. *Development*. 2000;127(13):2933-2943. doi:10.1242/dev.127.13.2933

57. Koyano-Nakagawa N, Kim J, Anderson D, Kintner C. Hes6 acts in a positive feedback loop with the neurogenins to promote neuronal differentiation. *Development*. 2000;127(19):4203-4216. doi:10.1242/dev.127.19.4203

58. Gratton MO, Torban E, Jasmin SB, Theriault FM, German MS, Stifani S. Hes6 promotes cortical neurogenesis and inhibits Hes1 transcription repression activity by multiple mechanisms. *Mol Cell Biol*. 2003;23(19):6922-6935. doi:10.1128/MCB.23.19.6922-6935.2003

59. Vias M, Massie CE, East P, et al. Pro-neural transcription factors as cancer markers. *BMC Med Genomics*. 2008;1:17. Published 2008 May 19. doi:10.1186/1755-8794-1-17

60. Qi J, Nakayama K, Cardiff RD, et al. Siah2-dependent concerted activity of HIF and FoxA2 regulates formation of neuroendocrine phenotype and neuroendocrine prostate tumors. *Cancer Cell*. 2010;18(1):23-38. doi:10.1016/j.ccr.2010.05.024

61. Carvalho FL, Marchionni L, Gupta A, et al. HES6 promotes prostate cancer aggressiveness independently of Notch signalling. *J Cell Mol Med*. 2015;19(7):1624-1636. doi:10.1111/jcmm.12537

62. Annala M, Kivinummi K, Leinonen K, et al. DOT1L-HES6 fusion drives androgen independent growth in prostate cancer. *EMBO Mol Med*. 2014;6(9):1121-1123. doi:10.15252/emmm.201404210

63. Wang Y, Xue H, Zhu X, et al. Deciphering the Transcription Factor Landscape in Prostate Cancer Progression: A Novel Approach to Understand NE Transdifferentiation. *Adv Sci (Weinh)*. Published online March 17, 2025. doi:10.1002/advs.202404938

64. Ramos-Montoya A, Lamb AD, Russell R, et al. HES6 drives a critical AR transcriptional programme to induce castration-resistant prostate cancer through activation of an E2F1-mediated cell cycle network. *EMBO Mol Med*. 2014;6(5):651-661. doi:10.1002/emmm.201303581

65. Ku SY, Rosario S, Wang Y, et al. Rb1 and Trp53 cooperate to suppress prostate cancer lineage plasticity, metastasis, and antiandrogen resistance. *Science*. 2017;355(6320):78-83. doi:10.1126/science.aah4199

66. Beltran H, Prandi D, Mosquera JM, et al. Divergent clonal evolution of castration-resistant neuroendocrine prostate cancer. *Nat Med*. 2016;22(3):298-305. doi:10.1038/nm.4045

67. Labrecque MP, Coleman IM, Brown LG, et al. Molecular profiling stratifies diverse phenotypes of treatment-refractory metastatic castration-resistant prostate cancer. *J Clin Invest*. 2019;129(10):4492-4505. Published 2019 Jul 30. doi:10.1172/JCI128212

68. Robinson D, Van Allen EM, Wu YM, et al. Integrative clinical genomics of advanced prostate cancer [published correction appears in Cell. 2015 Jul 16;162(2):454]. *Cell*. 2015;161(5):1215-1228. doi:10.1016/j.cell.2015.05.001

69. Morrissey C, Roudier MP, Dowell A, et al. Effects of androgen deprivation therapy and bisphosphonate treatment on bone in patients with metastatic castration-resistant prostate cancer: results from the University of Washington Rapid Autopsy Series. *J Bone Miner Res*. 2013;28(2):333-340. doi:10.1002/jbmr.1749

70. Nguyen HM, Vessella RL, Morrissey C, et al. LuCaP Prostate Cancer Patient-Derived Xenografts Reflect the Molecular Heterogeneity of Advanced Disease and Serve as Models for Evaluating Cancer Therapeutics. *Prostate*. 2017;77(6):654-671. doi:10.1002/pros.23313

71. Sharifi MN, Sperger JM, Taylor AK, et al. High-Purity CTC RNA Sequencing Identifies Prostate Cancer Lineage Phenotypes Prognostic for Clinical Outcomes. *Cancer Discov*. Published online April 1, 2025. doi:10.1158/2159-8290.CD-24-1509

72. Long X, Hou H, Wang X, et al. Immune signature driven by ADT-induced immune microenvironment remodeling in prostate cancer is correlated with recurrence-free survival and immune infiltration. *Cell Death Dis*. 2020;11(9):779. Published 2020 Sep 19. doi:10.1038/s41419-020-02973-1

73. Sharma NV, Pellegrini KL, Ouellet V, et al. Identification of the Transcription Factor Relationships Associated with Androgen Deprivation Therapy Response and Metastatic Progression in Prostate Cancer. *Cancers (Basel)*. 2018;10(10):379. Published 2018 Oct 11. doi:10.3390/cancers10100379

74. Wilkinson S, Ye H, Karzai F, et al. Nascent Prostate Cancer Heterogeneity Drives Evolution and Resistance to Intense Hormonal Therapy. *Eur Urol*. 2021;80(6):746-757. doi:10.1016/j.eururo.2021.03.009

75. Koppens M, van Lohuizen M. Context-dependent actions of Polycomb repressors in cancer. *Oncogene*. 2016;35(11):1341-1352. doi:10.1038/onc.2015.195

76. Cao J, Liu Z, Cheung WK, et al. Histone demethylase RBP2 is critical for breast cancer progression and metastasis. *Cell Rep*. 2014;6(5):868-877. doi:10.1016/j.celrep.2014.02.004

77. Teng YC, Lee CF, Li YS, et al. Histone demethylase RBP2 promotes lung tumorigenesis and cancer metastasis. *Cancer Res*. 2013;73(15):4711-4721. doi:10.1158/0008-5472.CAN-12-3165

78. Ikushima H, Miyazono K. Cellular context-dependent "colors" of transforming growth factor-beta signaling. *Cancer Sci*. 2010;101(2):306-312. doi:10.1111/j.1349-7006.2009.01441.x

79. Golias T, Papandreou I, Sun R, et al. Hypoxic repression of pyruvate dehydrogenase activity is necessary for metabolic reprogramming and growth of model tumours. *Sci Rep*. 2016;6:31146. Published 2016 Aug 8. doi:10.1038/srep31146

80. Liu Z, Yu M, Fei B, Fang X, Ma T, Wang D. miR-21-5p targets PDHA1 to regulate glycolysis and cancer progression in gastric cancer. *Oncol Rep*. 2018;40(5):2955-2963. doi:10.3892/or.2018.6695

81. Penugurti V, Mishra YG, Manavathi B. AMPK: An odyssey of a metabolic regulator, a tumor suppressor, and now a contextual oncogene. *Biochim Biophys Acta Rev Cancer*. 2022;1877(5):188785. doi:10.1016/j.bbcan.2022.188785

82. Wang Y, Guo YR, Liu K, et al. KAT2A coupled with the α-KGDH complex acts as a histone H3 succinyltransferase. *Nature*. 2017;552(7684):273-277. doi:10.1038/nature25003

83. Nagaraj R, Sharpley MS, Chi F, et al. Nuclear Localization of Mitochondrial TCA Cycle Enzymes as a Critical Step in Mammalian Zygotic Genome Activation. *Cell*. 2017;168(1-2):210-223.e11. doi:10.1016/j.cell.2016.12.026

84. Sivanand S, Rhoades S, Jiang Q, et al. Nuclear Acetyl-CoA Production by ACLY Promotes Homologous Recombination. *Mol Cell*. 2017;67(2):252-265.e6. doi:10.1016/j.molcel.2017.06.008

85. Li X, Yu W, Qian X, et al. Nucleus-Translocated ACSS2 Promotes Gene Transcription for Lysosomal Biogenesis and Autophagy. *Mol Cell*. 2017;66(5):684-697.e9. doi:10.1016/j.molcel.2017.04.026

86. Liu X, Si W, He L, et al. The existence of a nonclassical TCA cycle in the nucleus that wires the metabolic-epigenetic circuitry. *Signal Transduct Target Ther*. 2021;6(1):375. Published 2021 Nov 3. doi:10.1038/s41392-021-00774-2

87. Guertin DA, Wellen KE. Acetyl-CoA metabolism in cancer. *Nat Rev Cancer*. 2023;23(3):156-172. doi:10.1038/s41568-022-00543-5

88. Baksh SC, Finley LWS. Metabolic Coordination of Cell Fate by α-Ketoglutarate-Dependent Dioxygenases. *Trends Cell Biol*. 2021;31(1):24-36. doi:10.1016/j.tcb.2020.09.010

89. Jing Y, Ding D, Tian G, et al. Semisynthesis of site-specifically succinylated histone reveals that succinylation regulates nucleosome unwrapping rate and DNA accessibility. *Nucleic Acids Res*. 2020;48(17):9538-9549. doi:10.1093/nar/gkaa663

90. Zorro Shahidian L, Haas M, Le Gras S, et al. Succinylation of H3K122 destabilizes nucleosomes and enhances transcription. *EMBO Rep*. 2021;22(3):e51009. doi:10.15252/embr.202051009

91. Poli J, Tsaponina O, Crabbé L, et al. dNTP pools determine fork progression and origin usage under replication stress. *EMBO J*. 2012;31(4):883-894. doi:10.1038/emboj.2011.470

92. Shi DD, Savani MR, Abdullah KG, McBrayer SK. Emerging roles of nucleotide metabolism in cancer. *Trends Cancer*. 2023;9(8):624-635. doi:10.1016/j.trecan.2023.04.008

93. Wu HL, Gong Y, Ji P, Xie YF, Jiang YZ, Liu GY. Targeting nucleotide metabolism: a promising approach to enhance cancer immunotherapy. *J Hematol Oncol*. 2022;15(1):45. Published 2022 Apr 27. doi:10.1186/s13045-022-01263-x

94. Zhou W, Yao Y, Scott AJ, et al. Purine metabolism regulates DNA repair and therapy resistance in glioblastoma. *Nat Commun*. 2020;11(1):3811. Published 2020 Jul 30. doi:10.1038/s41467-020-17512-x

95. Zou S, Qin B, Yang Z, et al. CSN6 Mediates Nucleotide Metabolism to Promote Tumor Development and Chemoresistance in Colorectal Cancer. *Cancer Res*. 2023;83(3):414-427. doi:10.1158/0008-5472.CAN-22-2145

96. Mullen NJ, Singh PK. Nucleotide metabolism: a pan-cancer metabolic dependency. *Nat Rev Cancer*. 2023;23(5):275-294. doi:10.1038/s41568-023-00557-7

97. Crowell PD, Giafaglione JM, Hashimoto T, Diaz JA, Goldstein AS. Evaluating the Differentiation Capacity of Mouse Prostate Epithelial Cells Using Organoid Culture. *J Vis Exp*. 2019;(153):10.3791/60223. Published 2019 Nov 22. doi:10.3791/6022

98. Drost J, Karthaus WR, Gao D, et al. Organoid culture systems for prostate epithelial and cancer tissue. *Nat Protoc*. 2016;11(2):347-358. doi:10.1038/nprot.2016.006

99. Chambers MC, Maclean B, Burke R, et al. A cross-platform toolkit for mass spectrometry and proteomics. *Nat Biotechnol*. 2012;30(10):918-920. doi:10.1038/nbt.2377

100. Pluskal T, Castillo S, Villar-Briones A, Oresic M. MZmine 2: modular framework for processing, visualizing, and analyzing mass spectrometry-based molecular profile data. *BMC Bioinformatics*. 2010;11:395. Published 2010 Jul 23. doi:10.1186/1471-2105-11-395

101. Myers OD, Sumner SJ, Li S, Barnes S, Du X. One Step Forward for Reducing False Positive and False Negative Compound Identifications from Mass Spectrometry Metabolomics Data: New Algorithms for Constructing Extracted Ion Chromatograms and Detecting Chromatographic Peaks. *Anal Chem*. 2017;89(17):8696-8703. doi:10.1021/acs.analchem.7b00947

102. Su X, Lu W, Rabinowitz JD. Metabolite Spectral Accuracy on Orbitraps. *Anal Chem*. 2017;89(11):5940-5948. doi:10.1021/acs.analchem.7b00396

103. Dobin A, Davis CA, Schlesinger F, et al. STAR: ultrafast universal RNA-seq aligner. *Bioinformatics*. 2013;29(1):15-21. doi:10.1093/bioinformatics/bts635

104. Smyth GK. Linear models and empirical bayes methods for assessing differential expression in microarray experiments. *Stat Appl Genet Mol Biol*. 2004;3:Article3. doi:10.2202/1544-6115.1027

105. Tebon PJ, Wang B, Markowitz AL, et al. Drug screening at single-organoid resolution via bioprinting and interferometry. *Nat Commun*. 2023;14(1):3168. Published 2023 Jun 6. doi:10.1038/s41467-023-38832-8

106. Mudge JM, Carbonell-Sala S, Diekhans M, et al. GENCODE 2025: reference gene annotation for human and mouse. *Nucleic Acids Res*. 2025;53(D1):D966-D975. doi:10.1093/nar/gkae1078

107. Ewels P, Magnusson M, Lundin S, Käller M. MultiQC: summarize analysis results for multiple tools and samples in a single report. *Bioinformatics*. 2016;32(19):3047-3048. doi:10.1093/bioinformatics/btw354

108. Frelin, A.H., Zhu, H., and Boutros, P.C. (2024). OmicsQC: Nominating Quality Control Outliers in Genomic Profiling Studies. Version 1.1.0.

109. Li B, Dewey CN. RSEM: accurate transcript quantification from RNA-Seq data with or without a reference genome. *BMC Bioinformatics*. 2011;12:323. Published 2011 Aug 4. doi:10.1186/1471-2105-12-323

110. Wilke, C.O. (2024). cowplot: Streamlined Plot Theme and Plot Annotations for “ggplot2.” Version 1.1.3.

111. Barrett, T., Dowle, M., Srinivasan, A., Gorecki, J., Chirico, M., Hocking, T., Schwendinger, B., Krylov, I., Stetsenko, P., Short, T., et al. (2025). data.table: Extension of “data.frame.” Version 1.17.0.

112. Boutros, P., P’ng, C., Green, J., Prokopec, S., Research, O.I. for C., Team, T.R.C., Foundation, T.R., Gentleman, R., Ihaka, R., Bugh, C., et al. (2024). BoutrosLab.plotting.general: Functions to Create Publication-Quality Plots. Version 7.1.2.

113. R: The R Project for Statistical Computing https://www.r-project.org/.

114. Mootha VK, Lindgren CM, Eriksson KF, et al. PGC-1alpha-responsive genes involved in oxidative phosphorylation are coordinately downregulated in human diabetes. *Nat Genet*. 2003;34(3):267-273. doi:10.1038/ng1180

115. Subramanian A, Tamayo P, Mootha VK, et al. Gene set enrichment analysis: a knowledge-based approach for interpreting genome-wide expression profiles. *Proc Natl Acad Sci U S A*. 2005;102(43):15545-15550. doi:10.1073/pnas.0506580

116. Sud M, Fahy E, Cotter D, et al. Metabolomics Workbench: An international repository for metabolomics data and metadata, metabolite standards, protocols, tutorials and training, and analysis tools. *Nucleic Acids Res*. 2016;44(D1):D463-D470. doi:10.1093/nar/gkv1042

144

145

147

148

150

151